3 1211 00878202 7

UNIVERSITY LIBRARIES
NORTHERN ILLINOIS UNIVERSITY

NORTHERN ILLINOIS UNIVERSITY

SEARCH FOR THE FOURTH GENERATION QUARKS

A THESIS SUBMITTED TO THE GRADUATE SCHOOL

IN PARTIAL FULFILLMENT OF THE REQUIREMENTS

FOR THE DEGREE

MASTER OF SCIENCE

DEPARTMENT OF PHYSICS

BY

PRAJAKTA P. SINGH

DEKALB, ILLINOIS

AUGUST 1996

ABSTRACT

We present results on the search for the fourth generation quark (b'), which decays via flavor changing neutral currents (FCNC) into one photon. We have considered $b'\bar{b}'$ production in $p\bar{p}$ collision at center-of-mass energy of 1.8 TeV, with the integrated luminosity of 84.5 pb^{-1}. The subsequent decay of b' into a photon and jets with one b quark jet, is tagged by a soft muon. An analysis of this data gives the upper limit on Sigma x Branching Ratio at $m_{b'} = 100$ GeV/c^2 as 25.56 pb. This rules out the decay of b' via FCNC for $m_{b'}$ less than the Z mass, as the theoretically expected Sigma x Branching Ratio is 85.2 pb.

TABLE OF CONTENTS

Page

LIST OF TABLES vi

LIST OF FIGURES vii

CHAPTER 1. INTRODUCTION 1

A. b' Phenomenology 2

1. Direct Experimental Constraints on Fourth Generation Quarks 4

2. Indirect Constraints On Fourth Generation Quarks 4

3. Flavor Changing Neutral Currents Decay Modes Of The b' 5

4. b' Signatures and Backgrounds 6

CHAPTER 2. COLLIDER 7

CHAPTER 3. THE DETECTOR 11

A. The Central Detector 13

1. The Vertex Detector 15

2. The Transition Radiation Detector 15

3. The Central Drift Chamber 16

4. The Forward Drift Chamber 17

B. The Calorimeter 17

1. Operation Principles 19

Page

C. The Muon System 21

D. Data Sample And Trigger 22

CHAPTER 4. ANALYSIS 23

A. Triggers 23

1. Electromagnetic Triggers 23

2. Jet Triggers 24

B. Particle Identification 25

1. Photon Identification 25

a. EM fraction 25

b. Covariance Matrix χ^2 26

c. Isolation 32

2. Jet Identification 32

a. Jet E_T 35

3. Correction 35

a. EM Cluster Energy Correction 35

b. Jet Energy Correction 35

4. Tagging Muons 37

a. Muon Quality 37

b. Calorimeter Confirmation 37

C. Event Selection 39

1. Triggers 42

2. Photon Selection 42

3. Jet Selection 43

4. Tagging Muon Selection 43

5. H_T 48

Page

D. Acceptance 48

E. Background 48

1. Tag Rate Function 51

a. Tag rate η dependance 52

b. Tag rate E_T dependence 52

2. Background Calculation 55

CHAPTER 5. CONCLUSIONS 59

A. Cross Section And Mass Limits 59

BIBLIOGRAPHY 64

LIST OF FIGURES

Figure		Page
1-1	Weak decays of the b' quark:(a) charged current, (b) electroweak penguin, (c) box diagram.	3
1-2	Region of $m_{b'} - m_{t'}$ plane allowed by direct (thick line) and indirect experimental constraints at 95% CL (solid line) and 90% CL (dashed line).	5
2-1	The Tevatron At Fermilab	8
3-1	Cutway isometric view of the DØ detector.	12
3-2	A Side View Of The DØ Central Tracking System	14
3-3	An End-View Of One Quadrant Of The DØ Vertex Detector.	15
3-4	An End View Of One $\frac{3}{32}$ Of The DØ central Drift Chamber.	17
3-5	An Exploded Isometric View Of One Of The DØ Forward Drift Chamber.	18
3-6	A Cut-away View Of The DØ Calorimeter.	19
3-7	A Schematic View Of A Unit Cell Of The DØ Calorimeter.	20
4-1	EM fraction for photons in $\gamma + jets$.	26
4-2	EM fraction for electron in $Z \rightarrow e^+e^-$.	27
4-3	Comparison of EM fraction for photons and jets.	28

Figure Page

4-4 χ^2 for photons in $\gamma + 3jets$ events. 30

4-5 χ^2 for electrons in $Z \rightarrow e^+e^-$. 31

4-6 f_{iso} for photons in $\gamma + jets$ events. 33

4-7 f_{iso} for electrons in $Z \rightarrow e^+e^-$. 34

4-8 p_T distribution of tag muon for data. 38

4-9 p_T distribution of tag muon for ISAJET Monte carlo. 39

4-10 ΔR distribution for data. 40

4-11 ΔR distribution for ISAJET Monte Carlo. 41

4-12 E_T distribution for first, second and third jet for signal Monte Carlo ($m_{b'} = 100$GeV). 44

4-13 E_T distribution for first, second and third jet for data. 45

4-14 η distribution for all the jets for signal Monte Carlo ($m_{b'} = 100$GeV). 46

4-15 η distribution for all the jets for data. 47

4-16 Monte Carlo b' H_T distribution for several different b' masses. 49

4-17 Relative Significance as a function of the H_T cut for several different b' masses. 50

4-18 Tag rate per jet η dependence. 53

4-19 Tag rate per jet E_T dependence. 54

4-20 H_T distribution for various background. 56

4-21 H_T distribution of fake signal and background in bad photon + 3 jet events. 57

Figure **Page**

4-22 H_T distribution of data and background in photon + 3 jet events. The distribution can be compared to the the signal H_t distribution from monte-carlo in Fig. 4-16. 58

5-1 Comparison of measured cross section times branching ratio (points) and 95% CL upper limit (thick line) for $b'\bar{b}' \rightarrow \gamma$ + 3jets with the theoretical cross section of Laenen *et al.* times an assumed branching ratio of 18%. The dashed theory curve are upper and lower limit curve for the theoretical cross section. 62

5-2 Measured 95% CL upper limit on the branching ratio for $b'\bar{b}' \rightarrow \gamma$ + 3Jets assuming the theoretical cross section of Laenen *et al.*. The dashed curves are obtained using upper and lower limits on the cross section, rather than the central value. 63

CHAPTER 1
INTRODUCTION

The standard model (SM) describes the fundamental particles of nature and the interactions between them. In the SM description all matter is made up of two kinds of fundamental fermions- quarks and leptons. Both of them can further be classified into three families (also called generations). Each family is a replica of the others except that the particles in different families have different masses. Table 1-1 summarizes the classification of the fundamental particles of the SM. There are four kinds of interactions : electromagnetic, weak, strong and gravitational. The gravitational force between any two particles is so feeble compared to the rest that it can be safely ignored.

To take part in electromagnetic interactions (mediated by photons), a particle has to have electric charge. Photons couple with all fermions except the neutrino. Strong interactions (mediated by gluons) are limited to particles with color charge which is unique to the quarks and the gluons. The electromagnetic and the weak interactions have been unified in to the electroweak model.

Weak interactions are mediated by massive gauge bosons ($W^{\pm}$ and Z^0).The interactions involving $W^{\pm}$ are called charged current(CC).and involving Z^0 are called neutral currents.In SM decays like

$$W^+ \rightarrow u\bar{d} \quad or \quad W^- \rightarrow \bar{c}s(\text{ChargedCurrent})$$

$$Z^0 \rightarrow d\bar{d} \quad or \quad Z^0 \rightarrow b\bar{b}(\text{NeutralCurrent})$$

are allowed. Where as decays like $b \rightarrow s + Z^0$(Flavor Changing Neutral Current, FCNC , decays are suppressed by GIM mechanism [4].

Table 1-1. The fundamental particles in the Standard Model.

Particle class	Particle name	Spin	Charge	Mass (GeV/c^2)
Quarks	down(d)	$\frac{1}{2}$	$-\frac{1}{3}$	$\sim 0.35(\sim 5.6 \times 10^{-3})$
	up (u)	$\frac{1}{2}$	$+\frac{2}{3}$	$\sim 0.35(\sim 9.9 \times 10^{-3})$
	strange (s)	$\frac{1}{2}$	$-\frac{1}{3}$	$\sim 0.55(\sim 0.20)$
	charm (c)	$\frac{1}{2}$	$+\frac{2}{3}$	$\sim 1.6(\sim 1.35)$
	bottom (b)	$\frac{1}{2}$	$-\frac{1}{3}$	~ 4.5
	top (t)	$\frac{1}{2}$	$+\frac{2}{3}$	~ 180
Leptons	electron(e))	$\frac{1}{2}$	-1	5.11×10^{-4}
	e-neutrino(ν_e)	$\frac{1}{2}$	0	$< 7.3 \times 10^{-6}$
	muon (μ)	$\frac{1}{2}$	-1	0.1057
	μ-neutrino(ν_μ)	$\frac{1}{2}$	0	$< 2.7 \times 10^{-4}$
	tauon (τ)	$\frac{1}{2}$	-1	1.784
	τ-neutrino(ν_τ)	$\frac{1}{2}$	0	$< 3.5 \times 10^{-2}$
Gauge Bosons	gluons($g_i(i = 1...8)$)	1	0	0
	photon(γ)	1	0	0
	$W^\pm$	1	± 1	80.2
	Z	1	0	91.19
Higgs Boson	H^0	0	0	> 48

A. b' Phenomenology

The Standard Model, while being extremely successful, does predict neither the number of generations nor their mass spectrum. There remains a possibility for the existence of new particles which belong to new(fourth) generation.

Standard sequential fourth generation quarks(b', t') are pair -produced by the strong interaction with the same cross section for a given mass as the top quark [1], [2], [3]. SM weak decays of either quark can be produced via the charged current (CC)(Fig. 1-1(a)), or via loop-induced flavor changing neutral currents (FCNC) (Fig. 1-1(b),(c)). FCNC decay modes are far weaker than

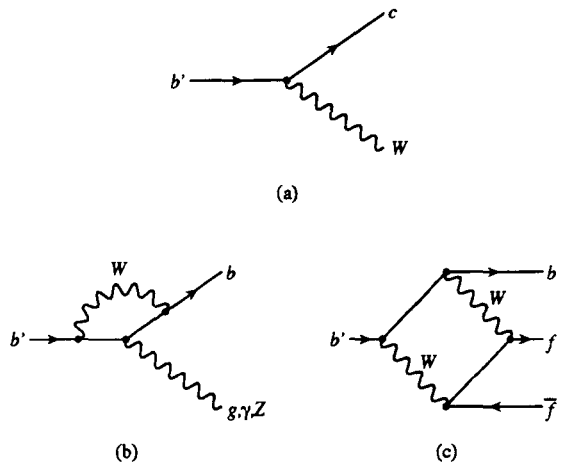

Figure 1-1. Weak decays of the b' quark:(a) charged current, (b) electroweak penguin, (c) box diagram.

corresponding CC decay modes due to the former being higher order in the weak interaction as well as possible suppression by GIM mechanism. It was realized in the late 1980's that a sufficiently light b' quark is unique in that it offers a plausible scenario for the weak FCNC decay to be the dominant decay mechanism [5]. If the b' quark is lighter than both t and t' quarks, then the CC decay to either is kinematically forbidden. In that case the dominant CC decay mechanism of b' is to the charm quark, which is however Cabibbo suppressed due to changing the generation number by two. In contrast the FCNC decay to the b quark is only required to change the generation number by one. Since b' FCNC decay diagrams are completely dominated by loops involving third and fourth generation quarks, GIM-type suppression will occur to the extent that the t and t' quarks are approximately degenerate. The relative strength of b' CC and FCNC decay will depend on the details of the CKM matrix and the t, b' and t' quark masses which are unknown(or not well known in the case of the t mass).

1. Direct Experimental Constraints on Fourth Generation Quarks

Fourth generation quarks that decay via the CC to bottom or charm quarks have experimental signatures that are very similar to top quark signatures that have been searched for by CDF and DØ. In particular, the dilepton and untagged single lepton signatures are basically identical. Only the b-tagged signature is not the same in the case of decay to the charm quark. The DØ mass limit of $M_t > 131$ GeV/c^2 [8], which did not make use of b-tagging, will apply with little modification to the lighter of b' or t', on the assumption of predominant CC decay. Direct searches for FCNC b' quark decay were carried out at e^+e^- colliders soon after the prediction of a substantial FCNC decay of the b' [9]. Limits are also obtained from measurements of R_{had} and the Z width. Here $R_{had} = \frac{\sigma \to q\bar{(q)}}{\sigma \to \mu^+\mu^-}$

The LEP data have ruled out b' with masses up to $m_Z/2$ regardless of decay mode [10].

2. Indirect Constraints On Fourth Generation Quarks

The most stringent indirect limit on the existence of fourth generation quarks comes from the ρ parameter ($\rho = m_W^2/(cos^2\theta_W)$). In the SM, ρ=1. Radiative corrections generate a positive contribution to form each non-degenerate weak isodoublet [11]:

$$\Delta\rho = \frac{G_F C}{8\sqrt{2\pi^2}}\Delta m^2 \tag{1-1}$$

where C is a color factor (i.e. C=3 for quarks), and Δm^2 is the mass splitting of the isodoublet and G_F is Fermi constant.Assuming that the interpretation of the observed top signals by CDF and DØ is correct, most of the known deviation of ρ from unity is accounted for by the large $m_b - m_t$ mass splitting. Any additional positive contributions to $\Delta\rho$ from fourth generation quarks and leptons, or other new particles, reduce the indirect upper limit on the top quark mass. Therefore, in order to avoid a large discrepancy between the predicted and measured value of ρ, a light b' quark also implies a relatively light t' quark. The allowed region in the $m_{b'} - m_{t'}$ plane is shown in Figure 1-2

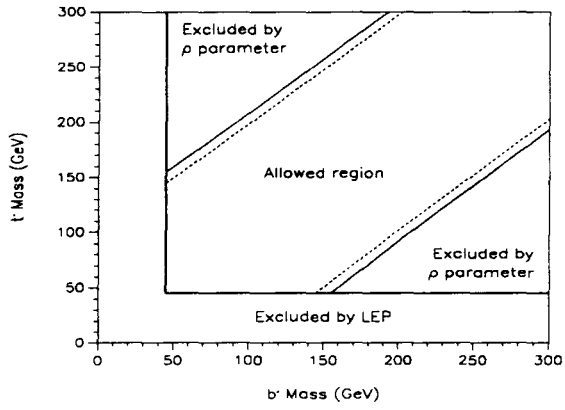

Figure 1-2. Region of $m_{b'} - m_{t'}$ plane allowed by direct (thick line) and indirect experimental constraints at 95% CL (solid line) and 90% CL (dashed line).

It has been suggested that t quark signatures observed by CDF and DØ are due to t' rather than t, and the third generation t quark itself is invisible because it decays by an exotic decay mode [12], [13].

3. Flavor Changing Neutral Currents Decay Modes Of The b'

The FCNC decay modes of the b' quark are generally to a b quark and a gauge boson or fermion pair:

$$b' \rightarrow bg$$

$$b' \rightarrow b\gamma$$

$$b' \rightarrow bZ^0$$

$$b' \rightarrow bH^0$$

The neutral Higgs boson decay mode can be the dominant decay mode if the H^0 is light enough. However the Higgs boson decay mode was not considered in the present search as its strength is strongly dependent on H^0 mass. The Z boson decay mode is predicted to be the dominant FCNC decay mode for

sufficiently heavy b', dominating even the gluon decay mode [14]. The Z decay modes are not considered in this thesis. In DØ the present search made use of only those signatures involving at least one photon or non-resonant lepton pair (e^+e^- or $\mu^+\mu^-$). In this thesis $b' \rightarrow b\gamma$ along with hadronic decay of b' is considered. Because of Z dominance, such signatures are limited to b' masses below approximately 120GeV/c^2,depending on the t' mass. The relative branching ratios of the various FCNC decay modes are calculable in the Standard Model [20] The branching ratio for

$$b' \rightarrow b\gamma$$

relative to all FCNC modes is approximately $\frac{\alpha}{\alpha_s}$ or about 10%.

4. b' Signatures and Backgrounds

$$b'\bar{b'} \rightarrow \gamma + 3jets + \mu - tag$$

This signature occurs when one b' decays to a photon and the second b' decays to a gluon or otherwise hadronically. The two main backgrounds to this signature are high p_T *photon* + jets production, and multijet production with a fake photon.

CHAPTER 2
COLLIDER

The Tevatron collider [22],[23] at Fermilab shown in Figure 2-1 consists of seven major components:

- A Cockroft-Walton accelerator(the Pre-accelerator).
- A linear accelerator(the Linac).
- The Booster synchrotron.
- The main ring synchrotron.
- The Antiproton Source.
- The Antiproton Debuncher.
- The tevatron Ring.

First H^- ions are created in an "ion source" by passing Hydrogen gas over a catalytic surface in the presence of free electrons. These ions are released into the pre-accelerator which produces a static electric field to accelerate the ions to 750 keV. The ions are then injected into the 150 meter long Linac. This device induces an oscillating electric field between a series of electrodes which accelerates the ions to 200 MeV. The H^- ions are then sent through a carbon foil which strips both the electrons off each ion. What comes out of the carbon foil are protons (H^+) ions. The protons are steered into the booster synchrotron ring (500 meters in circumference). A synchrotron is a cyclic accelerator in which the particles are confined to a closed orbit by a series of bending magnets. Quadruple focusing fields keep the beam from diverging. On each pass around the ring, the particle's energy is increased by acceleration

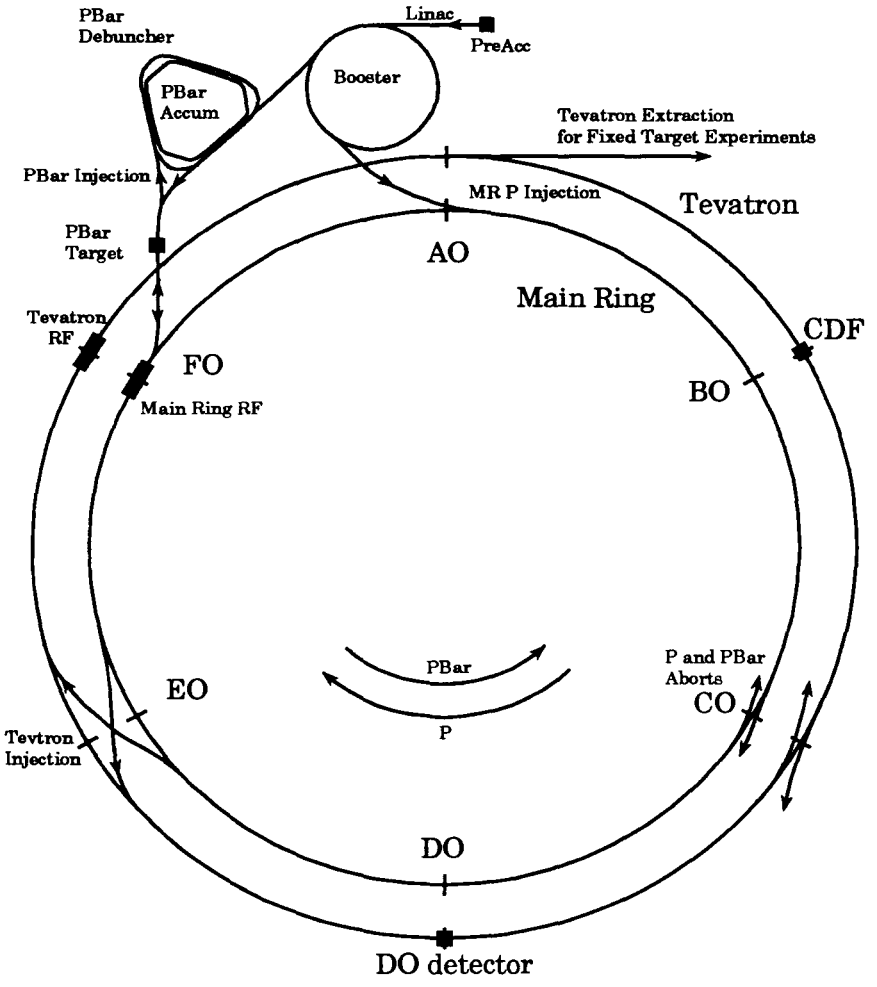

Figure 2-1. The Tevatron At Fermilab

in a set of synchronized Radio Frequency (RF) cavities. As the momentum increases, the magnetic field in the bending magnets must be increased to keep the particle in the ring: $p = qBr$ where p is the particle momentum, q its charge, B the magnetic field and r the radius of curvature. Protons exiting the booster have an energy of 8 GeV. These protons are injected in to the Main Ring (MR) which is a synchrotron consisting of more than 1000 conventional copper-coiled magnets in a ring 6km in circumference. The MR accelerates the protons and coalesces them in to shorter bunches. When the protons have attained 120 GeV, the bunches are extracted and directed onto a nickel/copper target creating about 2×10^7 antiprotons per bunch. A cylinder of liquid lithium creates a focusing magnetic field from a pulsed current of 600,000 amperes which keeps the antiproton beam from diverging. Following this treatment, the antiprotons are injected into the first of two antiproton storage rings.

This first ring is known as the "Debuncher" which uses sophisticated RF techniques to squeeze the antiprotons beam further into as compact a phase space as possible. This process is known as "cooling." The debuncher uses two cooling processes. The first is called "debunching." Fluctuation in the longitudinal component of the antiproton momenta is reduced by computer controlled RF manipulation. The second process is known as "stochastic cooling" which restricts the transverse oscillations of the antiproton beam. Fluctuations in the circulating current are detected by sensors which send correction signals to "kicker" electrodes which adjust path of the particle. When the process is complete, the antiprotons form a ring that looks almost static in a rotating frame of reference. These antiprotons are then transferred in to the antiproton storage ring known as the "Accumulator" 2×10^{10} at a time. The Debuncher and the Accumulator are in the same tunnel which is 520 meters in circumference. Several different system within the accumulator provide further cooling and increase the density of the antiprotons by a factor of about 10. It takes four to six hours for the antiproton population in the Accumulator to reach 2×10^{11} which is enough for a "shot" into the Tevatron.

Next the antiprotons are transferred to MR, accelerated to 150 GeV and then injected into the Tevatron, travelling in the direction opposite to that of protons. The Tevatron is in the same tunnel as the MR, but uses much

stronger superconducting magnets which, operating at a temperature of 4.7K, produce a field of $\approx$ 4 Tesla. In the final step six bunches of antiprotons and six bunches of protons are simultaneously raised to full energy, i.e. 0.9 TeV. At this energy the beams are squeezed very hard at two beam crossing points, B0 (CDF) and D0. Before the detectors start collecting data "scraping" is done in which halo and other debris from beam are removed. In scraping metal plates collimate the beam. The typical lifetime of a beam is approximately 20 hours after which its quality falls below the lowest acceptable standard. During this time the antiproton source runs continuously so that a stack of antiprotons is ready when the next shot is needed.

Luminosity for the colliders is defined as

$$L = n_1 n_2 f / A$$

Here

- n_1(or n_2) are number of particles(p or $\bar{p}$) per bunch
- A is the area of cross section of each bunch
- f is the frequency of bunch crossing.

.

The Integrated luminosity Collected by DØ in run1(1a+1b) of Tevatron is $\approx 100pb^{-1}$.

CHAPTER 3
THE DETECTOR

The DØ detector shown in Figure 3-1 has been constructed to study proton-antiproton collision at $\sqrt{s}$=2 TeV in the Tevatron collider. The various components of DØ detector have been discussed extensively in the literature [6]. The prime focus of the DØ experiment is to study high mass states and large p_T phenomena. This includes the search for the Top quark, the production of b quark hadrons as well as searches for new phenomena beyond the "Standard Model." The detector has the following features:

A) A compact non-magnetic central tracking system at the core. This system consists of four subdetectors and is known collectively as the Cental Detector. The CD traces the charged particle trajectories with adequate spatial resolution and offers measurements of the absolute charge (using $\frac{dE}{dx}$ in drift chambers) and the absolute charge-to-mass ratio of the particles.

B) A finely segmented thick sampling calorimeter which is the heart of the DØ detector and provides accurate energy measurements for photons, electrons, and jets, and the total transverse momenta of neutrinos and other non-interacting particles. It also offers confirmation for muons based on its trace of a minimum ionizing particle (MIP). The calorimeter forms the layer between the innermost CD and the outermost muon system.

C) A muon system with thick magnetized iron absorbers sandwiched between layers of proportional wire drift chambers. This allows momentum measurement for the muons. All of the above components require strong well-controlled electric fields to drive charged secondaries which carry all the available information on the primary to the readout channels in an orderly manner. Thus it is important to develop a high-voltage system that keeps the detector alive. The

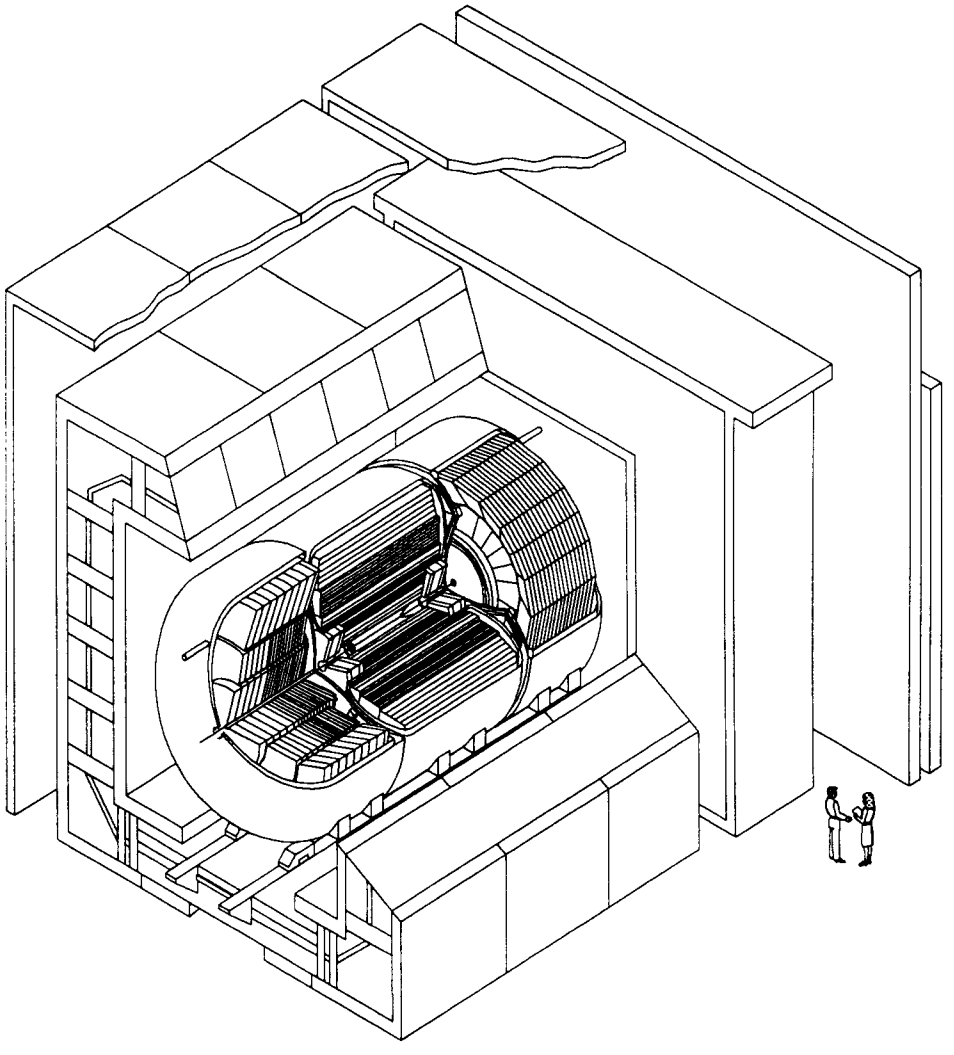

Figure 3-1. Cutway isometric view of the DØ detector.

information coming out from these channels at high rates requires a sophisticated data acquisition system (DAQ) to make efficient use of it. At DØ , this consists of 2 levels of online triggers that sequentially sift out the most interesting events and store them for offline scrutiny. We use the right-handed cylindrical coordinate system to describe the events at DØ. The direction of the protons defines z axis. The azimuthal axis is horizontal such that $\phi = \pi/2$ points vertically upward. The Rapidity is defined as

$$y = \frac{\ln(E + p_z)}{(E - p_z)} \tag{3-1}$$

and pseudorapidity is defined as

$$\eta = -\ln(\tan\theta/2) \tag{3-2}$$

For $M \ll E$, $\eta \approx y$ Vectors in the detector are usually defined by r, η and ϕ.

In the following section components of the DØ detector crucial for this analysis are described.

- Central detectors are used for vertex reconstruction and μ track information.
- Calorimeters are used for the photon and jet identification and their energy measurement.
- Muon chamber information along with the information provided by calorimeters and central detectors is used for identifying the muons in the event.

A. The Central Detector

The central Detector (CD) is a nonmagnetic tracking system and consists of the vertex drift chamber (VTX), the transition radiation detector (TRD), the central drift chamber (CDC) and two forward drift chambers (FDC) as shown in Figure 3-2.

The VTX, TRD and CDC are concentric with the beam pipe and cover a large angular region. The FDCs are oriented perpendicular to the beam axis. All central detectors are located within the boundary, r=78 cm and z=$\pm$135 cm which is restricted by the inner radius of the calorimeter.

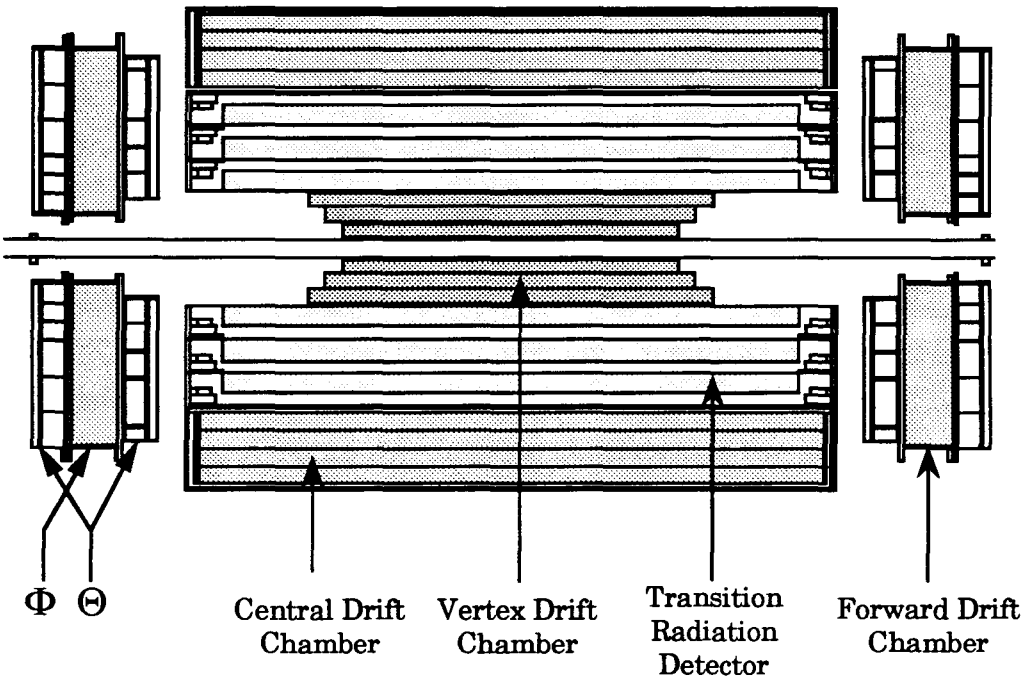

Figure 3-2. A Side View Of The DØ Central Tracking System .

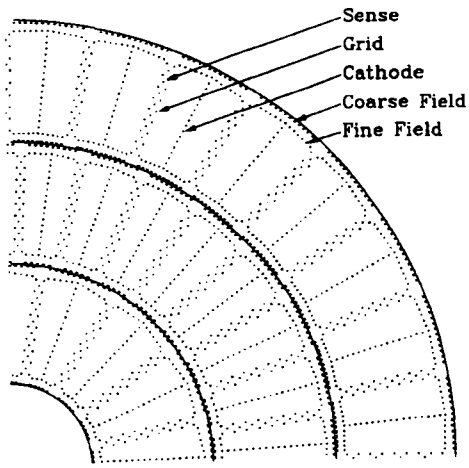

Figure 3-3. An End-View Of One Quadrant Of The DØ Vertex Detector.

1. The Vertex Detector

The VTX chamber is the innermost tracking detector which has an inner radius of 3.7 cm and outer radius of 16.2 cm. It consists of three independent concentric layers of cells as shown in Figure 3-3 mounted on carbon fiber tubes. The innermost layer has 16 cells in azimuth, the outer two layers have 32 cells. The sense wire provides a measurement of the z coordinate from readout at both ends. The electrostatic properties of the cell are determined by the grounded planes of grid-wire, sense wire planes, and the cathode field wire planes. To obtain good spatial resolution and track pair resolving power a gas mixture of CO_2(95%)-ethane(5%) at 1 atm with a small admixture of H_2O was chosen.

The typical position resolution of VTX detector is $50\mu m$.

2. The Transition Radiation Detector

The TRD is located between the VTX and the CDC, and provides independent electron/pion separation in addition to that given by the calorimeter.

Transition radiation x-rays are produced when highly relativistic charged particles ($\gamma >> 1$) traverse boundaries between media with different dielectric constants. The energies of radiated x-rays depend on the mass of a charged particle since the velocities of particles in media depend upon its mass. The TRD consists of three separated units, each containing a radiator and an x-ray detection chamber. The energy spectrum of the x-ray, determined by the thickness of the radiator foil and the gap between the foils, peaks at 8 keV and is mainly contained below 30 keV. A two-stage proportional wire chamber (PWC) is mounted just after the radiator for the detection x rays. The x-rays convert mainly in the first stage of the chamber and the resulting charge drifts radially outward to the sense wire.

Measures of the difference between electron and hadron include the total collected charge on anode wires, the number of charge clusters and the position of clusters determined through the time of arrival at the anodes. Pion rejections of the order of 50 are found for 90% efficiency for electrons in TRD. Rejection factors are better at non-normal incidence, because of the increased path length and due to space charge distortions at normal incidence induced by pile of all ionization along a particular track. The TRD information was not used in the analysis presented in this thesis.

3. The Central Drift Chamber

The CDC is located just after the TRD and just before the inner cylinder of the calorimeter. It consists of four concentric layers of drift chambers and each layer has 32 azimuthal cell as shown in Figure 3-4. Each cell contain seven sense wires with readout on one end and two delay lines with a redout on both ends. The delay lines propagate the signals induced from the neighboring anode wire; the difference of the arrival times at both ends provides the z-coordinate of the track. The CDC is operated with Ar(92.5%) CH_4(4%) CO_2 (3%) gas with 0.5%H_2O.

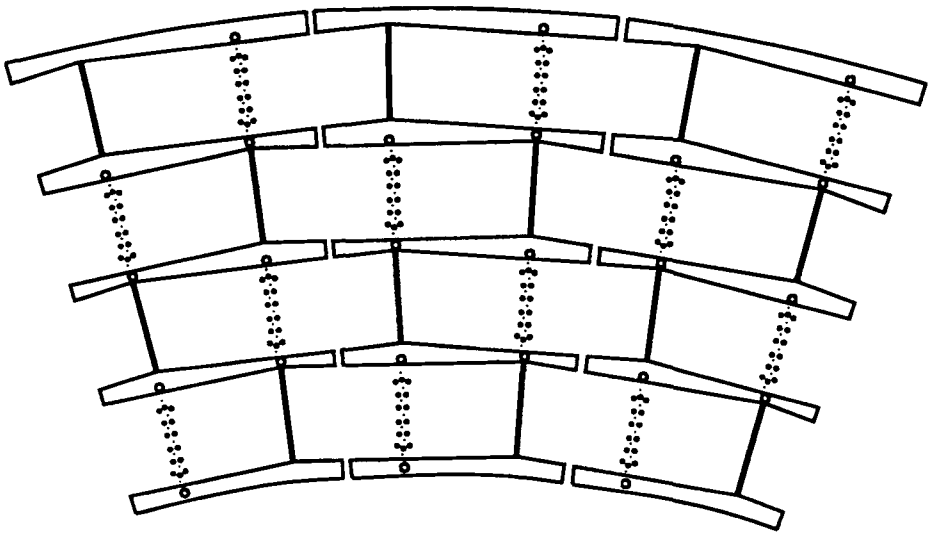

Figure 3-4. An End View Of One $\frac{3}{32}$ Of The DØ central Drift Chamber.

4. The Forward Drift Chamber

The FDCs extend the tracking coverage out to $|\eta| \approx 3$ They are positioned at both ends of the concentric barrels of the VTX, TRD and CDC as shown in Figure 3-5. Each FDC consists of three separate chambers, one phi module and two theta modules, which provide phi and theta coordinates depending upon the directions of their sense wires.

The typical position resolution in the CDC and FDC vary between 150 – $200\mu m$.

B. The Calorimeter

The purpose of a calorimeter is to measure energy. In particle detectors, calorimeter measure the energies of various particles. Liquid argon and depleted uranium are the active and passive (absorber) materials in DØ calorimeter. It consists of three cryostat systems, a central calorimeter (CC) and two end-cap

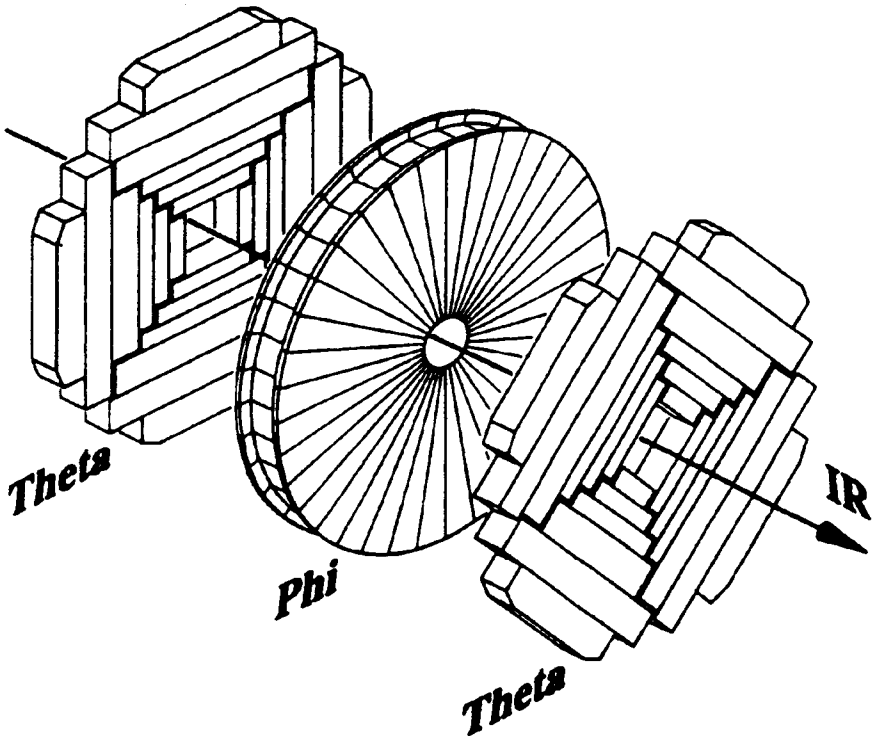

Figure 3-5. An Exploded Isometric View Of One Of The DØ Forward Drift Chamber.

calorimeters (EC),as shown in Figure 3-6. Since there is no central magnetic field, the DØ calorimeter plays important roles in the identification of high p_T objects, electrons, photons, jets and muons and providing the missing transverse energy. Each cryostat calorimeter consists of three distinct types of calorimeter modules: an electromagnetic section (EM) with relatively thin uranium absorber plates, a fine hadronic section (FH) and a coarse hadronic section (CH) with thick copper or stainless steel plates.

1. Operation Principles

A typical unit cell of the calorimeter consist of a uranium plate and a readout board submerged in liquid Argon(LAr) as shown in Figure 3-7. The readout board consist of two separate 0.5 mm thick G-10 boards, one side of which is

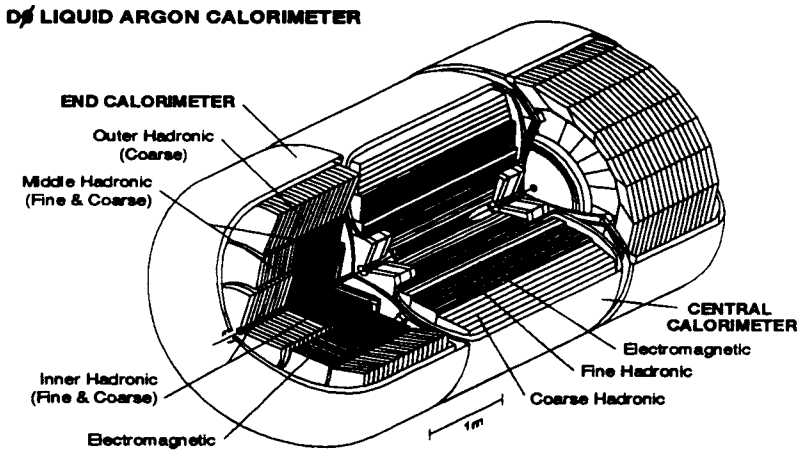

Figure 3-6. A Cut-away View Of The DØ Calorimeter.

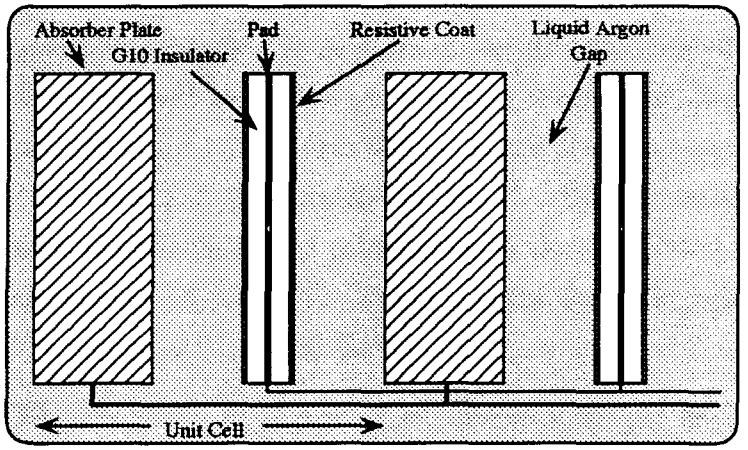

Figure 3-7. A Schematic View Of A Unit Cell Of The DØ Calorimeter.

coated with high resistivity epoxy. One of the inner surfaces is bare G-10; the other inner surface is copper-coated. These two G-10 boards were laminated with the resistance coats facing outwards. An electric field is formed by grounding the metal absorber plate and connecting the resistive surface of the readout board to positive high voltage. Thus the resistive surfaces act as an anode and the readout board operates as a capacitor.

When a high energy particle goes through dense material, e.g. uranium, a shower of particles occurs via various electromagnetic and hadronic interactions These particles ionize the active material via electromagnetic interactions. These ionized particles drift to the anode under the influence of the electric field and induce an image charge on the inner copper surface. This charge is routed to external charge-sensitive preamplifiers and subsequently to baseline subtracter (BLS) which are shaping and sampling hybrid circuits. The baseline and the peak of the signal are sampled in the circuit and their difference is sent to an analog-digital converter (ADC), the output of which is brought to a computer. If signal values are within a given range (± 2 sigma) of their pedestal

values, their channels are suppressed to reduce the quantity of the output data.

The calorimeter position resolution is important for identification of backgrounds to electrons from the near-overlap of photons and charge particles. This resolutions varies between 0.8 and 1.2mm over the full range of impact positions. The positions resolutions varies approximately as $1/\sqrt{E}$. The resolution and the linearity of response obtainable in the calorimeter is closely related to the ratio of response of electrons and pions [7]. The e/π response ratio falls from about 1.11 at 10 GeV to about 1.04 at 150 GeV.

The relative energy resolution for electrons and pions obtained after subtraction of pedestals, and after corrections for gain variations and beam particle momentum can be parameterized as

$$(\sigma_E/E)^2 = C^2 + S^2/E + N^2/E^2$$

Where C, S and N are constants representing the calibration errors, sampling fluctuations and noise contributions. We obtain $C = 0.003 \pm 0.002$ and $S = 0.157 \pm 0.005\sqrt{GeV}$ for electrons.

C. The Muon System

The DØ muon detection system consists of solid-iron toroidal magnets and three layers of proportional drift tube chamber (PDTs). The layer of PDT chambers inside the toroidal magnets has four drift planes. The other two layers have three planes each and are located outside the magnet. The purpose of this system is to identify muons produced in proton-antiproton collisions and measure their momenta. The muon system is divided into two sub-systems, wide angle muon chambers (WAMUS) covering the central region ($\eta_d < 2.5$) and small angle muon chambers (SAMUS) covering $2.5 < \eta_d < 3.6$. The toroidal magnets are also separated into five parts : A central toroid covering the region $|\eta_d| < 1.0$, two end toroids for $1 < |\eta_d| < 2.5$ and two SAMUS toroids covering $2.5 < |\eta_d| < 3.6$. Since a muon must traverse the calorimeter and the thick toroidal magnet, it requires a minimum momentum of 3.5GeV/c at $|\eta| = 0$ and about 5GeV/c at larger $|\eta|$.

The muon momentum p is measured from its deflection angle in the magnetic field of the toroid. The resolution for $1/p$ is approximately gaussian and given by $\sigma(1/p) = 0.18(p-2)/p^2 \oplus 0.008$ (with p in GeV/c).

D. Data Sample And Trigger

The DØ trigger has three levels in order to select and record interesting physics and calibration events. The Level 0 scintillation counters indicate the occurrence of an inelastic collision. At a luminosity of $L = 5 \times 10^{30}$, the Level 0 rate is about 150kHz. The Level 1 trigger is a collection of hardware trigger elements using signals from all subdetectors. Most of the Level 1 hardware triggers operate within the $3.5\mu sec$ time interval between beam crossings and do not contribute deadtime. Some of the Level 1 triggers require longer operation time and are referred to as level 1.5 triggers. The Level 1 trigger rate is around 200 Hz. After Level 1 the data are brought to a farm of microprocessors through the standard DØ data acquisition pathways. The farm of microprocessors, Level 2, reconstructs the data and selects event to reduce the event rate to about 2 Hz.

The data sample for this analysis comes from Runs Ia and Ib. The data samples for each run come from a single level 2 electron or photon trigger. The total integrated luminosity of the data sample used for this analysis is 84.5pb^{-1}. The entire data sample, including all of the run Ia data was reconstructed using DØ event reconstruction program.

CHAPTER 4
ANALYSIS

A. Triggers

DØ has a multilevel trigger system to reduce the event rate from the beam crossing frequency (286 kHz) to the rate at which events can be written to tape ($\approx 2Hz$). The triggers used for the $b'\bar{b}'$ searches are defined in terms of electromagnetic clusters and jets required in the level 1 and level 2 triggers.

1. Electromagnetic Triggers

A definition of an electromagnetic cluster at the first trigger (level 1) is based on trigger towers which sum the energy deposited in four electromagnetic compartments of a transverse area of (0.2×0.2 in $\eta \times \phi$ space). The measured energy is converted into the transverse energy which is defined as $E_T = E \sin\theta$ where E is the measured energy and θ is the angle between the trigger tower and the proton direction. The center of a tower is used to define an angle by which the energy deposition has to be weighted. A threshold is imposed on the transverse energy measured in a trigger tower. Trigger towers which satisfy the threshold requirement are called electron/photon candidates. At level 1 the threshold for electromagnetic clusters for triggers used in this analysis was set at 10 GeV during run Ib.

Electron/photon candidates are further processed at the second level of a trigger (level 2). Full calorimeter information (all channels) as well as the tracking information are available at this level. The electromagnetic cluster at this level is defined by two containment conditions , longitudinal and transverse. The longitudinal condition is defined as the electromagnetic component of a

shower constituting 90%-98% of the total shower energy where the total shower energy is defined as the sum of energies deposited in the four electromagnetic layers and the first hadronic layer.

The transverse condition is based on a pattern of energy deposition in the third electromagnetic layer which holds the peak of an average shower. This peak cell defines an outer area of dimension (0.25×0.25) in η and ϕ, and an inner area of dimension (0.15×0.15) in η and ϕ. The transverse condition requires that at least 80%-95% of energy detected in the outer area is also contained in the inner area.

2. Jet Triggers

Level 1 jet triggers require the sum of the transverse energy in the EM (electromagnetic) and FH (front hadronic) sections of a trigger tower to be above a programmed threshold (generally 3 GeV).

The level 2 jet algorithm begins with an E_T(transverse energy) ordered list of towers that were above threshold at level 1. At level 2 a jet is formed by placing a cone of given radius R, where $R = \sqrt{\Delta\phi^2 + \Delta\eta^2}$, around the seed tower from level 1. If another seed tower lies within the jet cone then it is passed over and not allowed to seed a new jet. For triggers used in the b' search we use jet cones with radius $R = 0.7$. To filter events, cuts on the following quantities can be imposed.

- The minimum transverse energy of a jet.
- The minimum transverse size of a jet.
- The minimum number of jets.
- psuedorapidity of the jets.

B. Particle Identification

The identification of an object is done at various stages. First, a preliminary tagging of candidates is done online by the trigger framework. Offline, the first pass on the reconstruction of an event is performed by a software package called "DØRECO" which first converts the electronic signals into measurements in position and momentum space. Then it identifies various physical entities such as electrons, photons, muons, jets and neutrinos in the event using those measurements. The final definition of an object in terms of the observed signatures depends on the topics of interest. The nature, cross section and understanding of the signal and background processes determine the optimal set of cuts. We will give the definition of each object relevant to us starting with the trigger we use.

1. Photon Identification

Photons are identified by the detection of an EM shower in the calorimeter with no associated track in the central tracking system. EM showers are characterized by making a comparison of the longitudinal and transverse profiles in the EM calorimeter to simulated EM showers. The first step in photon identification is the formation of clusters of adjacent EM calorimeter towers with significant energy depositions using a nearest neighbor clustering algorithm. The EM shower characteristics for electrons and photons should be identical. The difference in various distributions for photons from $\gamma + jets$ events and electrons from Z events indicate that there is some contamination from jets in the photon sample. The variables used in this analysis are described below.

a. EM fraction.

This is a very powerful cut which provides good discrimination against charged hadrons. The EM fraction is defined as

$$\frac{Energy\ in\ layers\ EM1 + EM2 + EM3 + EM4}{Energy\ in\ layers\ EM1 + EM2 + EM3 + EM4 + Hadronics} \tag{4-1}$$

and it is required that it be $\geq 95\%$. Figures 4-1 and 4-2 shows the EM fraction distribution for photons in $\gamma + jets$ events and electrons in $Z \rightarrow e^+e^-$ events respectively . Figure 4-3 shows comparison of EM fraction for photons and jets.

b. Covariance Matrix χ^2.

To quantify how well the pattern of energy deposition in a shower conforms to that expected of an electron or a photon we calculate its χ^2 with respect to a covariance matrix calibrated on Monte Carlo photons. The matrix elements

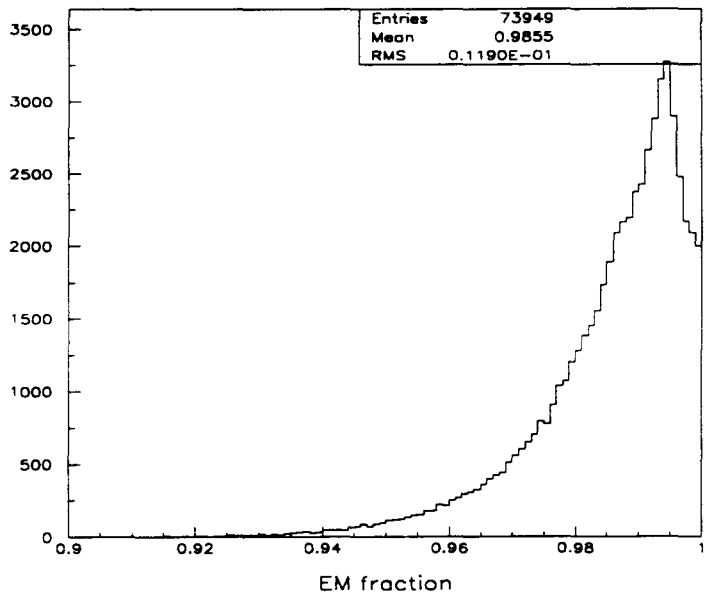

Figure 4-1. EM fraction for photons in $\gamma + jets$.

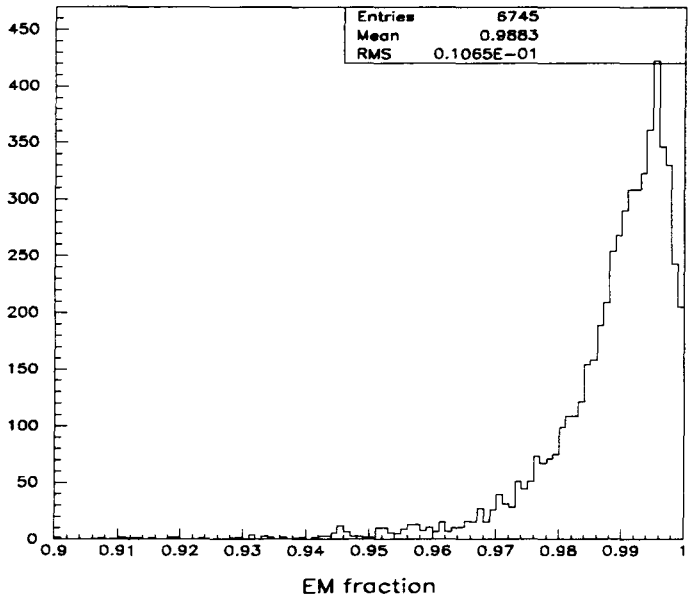

Figure 4-2. EM fraction for electron in $Z \rightarrow e^+e^-$.

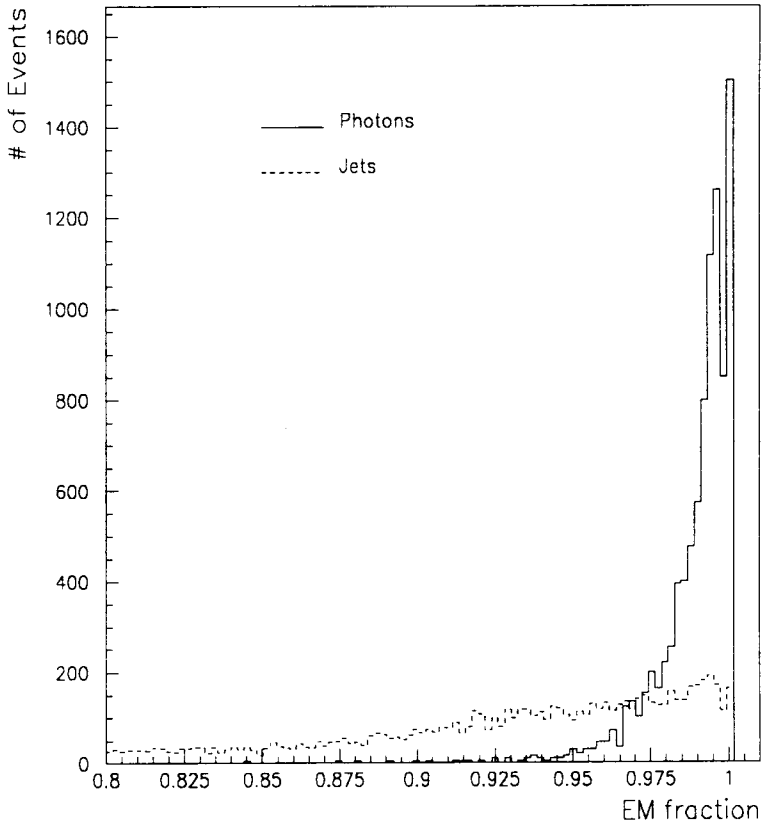

Figure 4-3. Comparison of EM fraction for photons and jets.

M_{ij} are defined as

$$M_{ij} = \sum_{n=1}^{n}(x_i^n - \bar{x}_i)(x_j^n - \bar{x}_i) \tag{4-2}$$

where x_i^n is the value of the ith variable for the nth photon and $\bar{x}_i$ is mean of ith variable. The 41 variables used are the fractional energies in layer 1, 2, 4 of the EM calorimeter, the fractional energy in each cell of a 6×6 array of cells in layer 3 centered on the most energetic tower in the EM cluster, the logarithm of the cluster energy and z position of the event vertex. Using this matrix the covariance parameter

$$\chi^2 = \sum_{ij}(x_i - \bar{x}_i)H_{ij}(x_j - \bar{x}_i) \tag{4-3}$$

can be used as a measure of the consistency of the shape of any data shower with respect to the shower shape of the N Monte Carlo $\gamma + 3jets$. Here $H = M^{-1}$ and x_i are the 41 variables used to characterize the shower.

In general, the values of the variables x_i are not normally distributed and therefore the covariance parameter χ^2 does not follow a normal distribution.H is a symmetric matrix and can diagonalize using an appropriate unitary matrix U. The χ^2 is then given by

$$\chi^2 = yHy^T \tag{4-4}$$

so that the transformed matrix $H' = U^T HU$ and the components of the vector y are uncorrelated variables. Components of y which dominate the value of χ^2 can be limited to a maximum value which will maximize the $\gamma + 3jets$ efficiency.

The χ^2 is thus a measure of how well the EM shower matches the characteristics of electron or photon. A reasonably good $\chi^2(< 100)$ is required for EM shower to characterized as coming from electron or photon.

Figures 4-4 and 4-5 show the distribution of χ^2 for $\gamma + 3jets$ and $Z \rightarrow e^+e^-$ respectively.

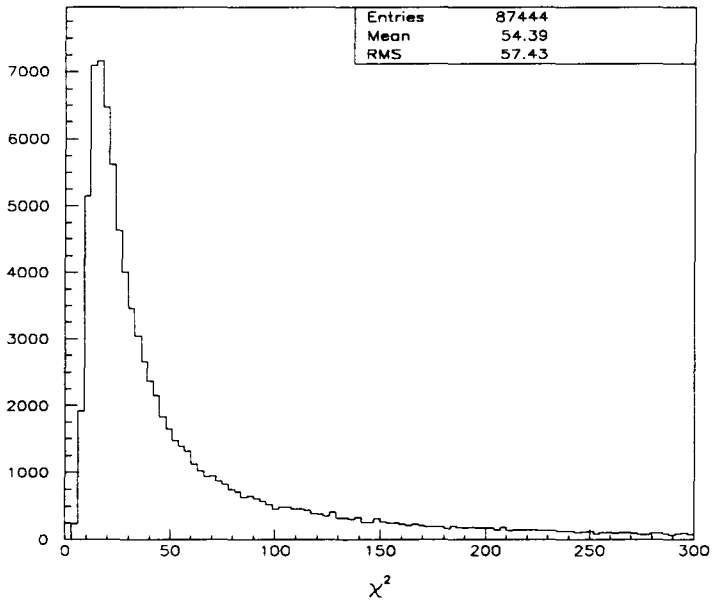

Figure 4-4. χ^2 for photons in $\gamma + 3jets$ events.

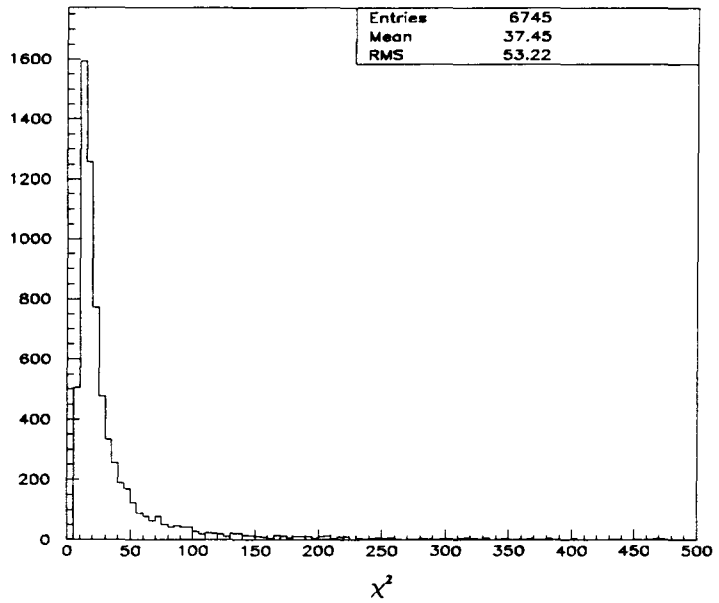

Figure 4-5. χ^2 for electrons in $Z \rightarrow e^+e^-$.

c. **Isolation.**

The isolation variable for an EM cluster is defined as

$$f_{iso} = \frac{E(0.4) - EM(0.2)}{EM(0.2)} \tag{4-5}$$

where $E(0.4)$ is the energy deposited in the cone $R < 0.4$,

and EM(0.2) is the EM energy in the cone $R < 0.2$. This variable is good for making cuts on electron/photons in processes where they are expected to be isolated. Figures 4-6 and 4-7 show the distribution of f_{iso} for $\gamma + jets$ and $Z \rightarrow e^+e^-$ events respectively.

The photon distributions for isolation, χ^2 and EM fraction are slightly worse than the electrons from Z decay, as the background content in the photon sample is much more than that in the Z sample, and a jet has more probability of being misidentified as a photon than being misidentified as an electron.

2. Jet Identification

Two types of algorithms are used in DØ to define jets. One is the nearest neighbor algorithm and the other one is the cone algorithm with various values of R,the radius of the cone in η, ϕ space. Calorimeter towers with a minimum E_T of 1 GeV are ordered in E_T and starting from the highest E_T tower preclusters are formed by including contiguous cell out to a radius of 0.5 (in η, ϕ space). These contiguous cells should have an E_T of at least 1GeV to be included in the preclusters. The formation of preclusters cuts down on the number of towers which can be considered a possible starting point for jet formation. The center of the precluster is considered the center of the cone jet. All towers within a radius of R from the center are included in the jet and a new E_T weighted center is calculated. This procedure of finding the new center is repeated until the jet center is stable. When jets share energy they are combined or split depending upon the fraction of energy shared relative to the lower jet E_T. If the fraction is less than 0.5 they are split, otherwise they are combined.

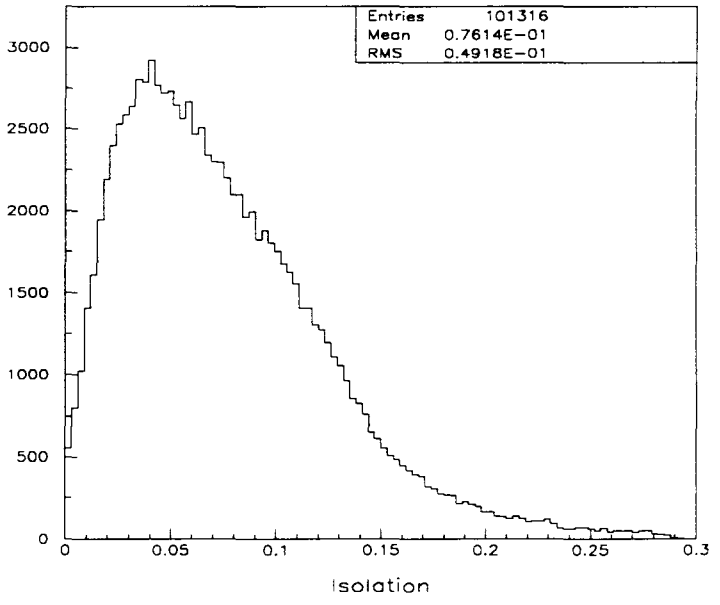

Figure 4-6. f_{iso} for photons in $\gamma + jets$ events.

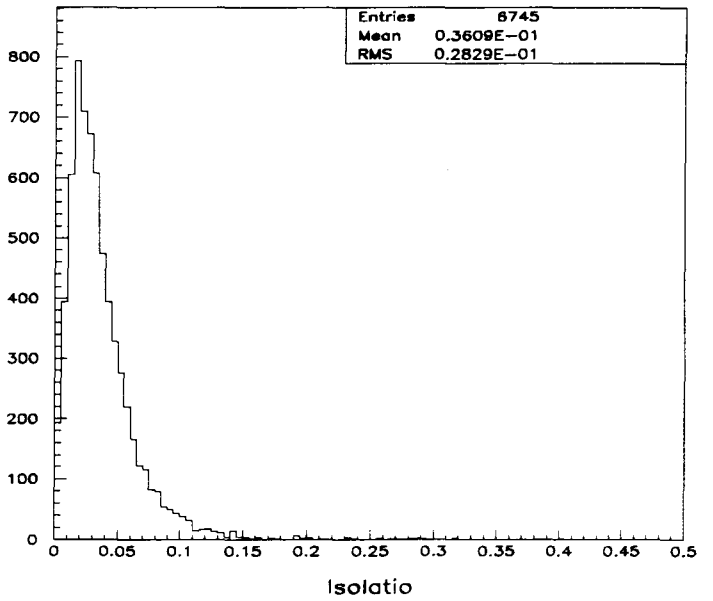

Figure 4-7. f_{iso} for electrons in $Z \rightarrow e^+e^-$.

a. Jet E_T.

The total transverse energy is defined as sum of the transverse electromagnetic energy and the transverse hadronic energy, $E_T = EM_T + H_T$ where EM_T is the transverse electromagnetic energy and H_T is the transverse hadronic energy.

3. Correction

In order to put the measured energies of the physics objects of interest in both the data and the Monte Carlo events on an equal footing, we apply a series of energy corrections to the EM clusters and jets.

a. EM Cluster Energy Correction.

The EM section sets the absolute energy scale or the DØ calorimeter. The EM energy scale is established by setting the invariant mass peak reconstructed from dielectron events in the appropriate mass region equal to Z mass . By requiring both electrons in same cryostat, we obtain an independent absolute scale factor for each cryostat [16] which we apply to isolated electron and photons.

b. Jet Energy Correction.

The correction for jet energies is more complicated. A jet is not a single particle, but a large collection of particles and most of them are at low momenta. For example, 70% of the energy of a centrally produced 50 GeV jet is made up of by particles with individual momentum less than 5 GeV. Because of nonlinearities in the response, especially at particle energies below 10 GeV, and variations in the response due to poorly instrumented regions, the measured jet energy has to be corrected to get the true jet energy. Here we define the true jet energy (E^c) as the energy of all particles contained in a cone $\Delta R = 0.5$ around the jet axis. The measured jet energy (E^m) is the energy determined in the calorimeter using the single particle response and a cone of size $\Delta R = 0.5$. The

corresponding transverse jet energies are defined as E_T^m and E_T^c. The current correction technique is based on using collider data only.

There are several effects which contribute to the jet energy response: nonuniformities in the calorimeter, nonlinearities in the calorimeter response to hadrons, noise due to radioactivity of the uranium and energy from the soft interaction of spectator partons within the protons and the antiprotons (underlying events). These effects have been estimated using collider data, monte carlo simulations and test beam data.

In central region ($|\eta| \leq 0.7$) a variant of the method described in [15] is used to measure the cumulative response of the calorimeter to the fragmentation products associated with jets. This method uses events with isolated EM clusters due to photons or jets which fragmented mostly into neutral mesons and at least one more hadronic jet. We attribute any energy imbalance along the direction of the photon in the transverse plane to the mismeasurement of the hadronic jet. In this way we measure the response of the calorimeter to the hadronic jet relative to the known response to the EM cluster.

The fragmentation products from final state partons falling within the jet cone produce wide showers in the calorimeter, causing some of energy to fall outside of the cone. To measure this out of cone fraction, we have substituted single particle test beam showers for fragmentation products in the monte carlo event generators ISAJET [17] and HERWIG [18]. We correct only for the energy deposited outside the jet cone due to showering, not for any particle landing out of the cone due to fragmentation or radiation.

Having obtained the corrections described above, for jets in the central calorimeter, we determine the variation of the jet energy scale with η and with the fraction of energy in the EM calorimeter by using dijet events. We determine these variations by balancing one jet in the forward region or a jet of varying EM fraction with an average jet in the central calorimeter.

Energy from the underlying event within the jet cone is included in the jet energy. The energy flow from the underlying event is assumed to be independent of the hard scatter that gives rise to the jets we observe [19]. We estimate this energy deposition by measuring the energy density in the minimum bias events

and then subtracting it from the jet energy. This also compensates for the biases in the energy measurement due to radioactivity of uranium.

4. Tagging Muons

The $b'\bar{b}'$ events which decay according to the photon + jets signature includes two b quarks with other decay products. Each b hadron can either decay semileptonically into a muon with a branching fraction of about 10% or decay sequentially into a muon. The processes that are the main background to the photon + jets signature are much less rich than $b'\bar{b}'$ in heavy flavor quarks and the resulting muons. Muon tagging provides an effective method of reducing the background and improving the signal to background ratio in the photon + jets b' search.

Muons arising from b quark decay have higher momenta than muons arising from $\pi - K$ decay . These muons are found in close proximity to jets. Figures 4-8 and 4-9 show the muon p_T distribution of tag muons for data and *ISAJET* Monte Carlo. Figures 4-10 and 4-11 show the muon jet separation in ΔR for data and *ISAJET* Monte Carlo.

The variables used to identify tagging muon in this analysis are:

a. Muon Quality. The muon reconstruction algorithm defines a muon track "quality" which contains information about the number of muon modules with recorded hits. If a track does not have the minimum number of hits on the fitted track, then it is determined to have the insufficient quality and is rejected. The number of failures in the local track fit in both the bend and non-bend view are stored in variable IFW4.

b. Calorimeter Confirmation. In traversing the calorimeter a muon deposits ionization energy in cells along its path. The muon reconstruction program reconstructs the muon track in the calorimeter and stores a set of parameters defining its quality.

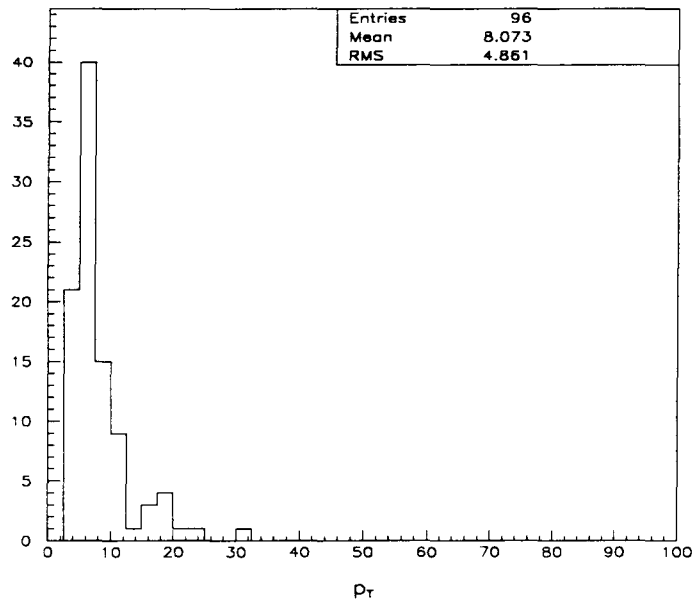

Figure 4-8. p_T distribution of tag muon for data.

The variable HFRAC is the fraction of all possible hadronic calorimeter layers utilized in the reconstructed muon track in calorimeter. For most trajectories the maximum number of layers is 4 although it may be equal to 3 or 5. We require HFRAC ≥ 0.75 , i.e. the allowed values of HFRAC are 3/4, 4/5 and 1.

The variable EFRAC_H(1:3) contains the fraction of energy deposited in the last, last two and last three layers.

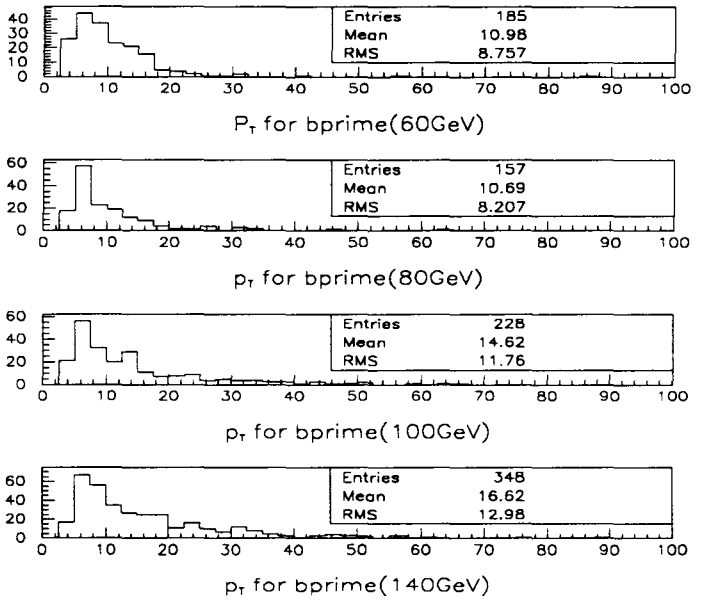

Figure 4-9. p_T distribution of tag muon for ISAJET Monte carlo.

C. Event Selection

The event selection criteria imposed on the reconstructed events were chosen to maximize the efficiency and minimize the background. The triggers and selection cuts on photon, jets and tagging muons used in the analysis are given below. This is followed by the the description of the kinematic cuts.

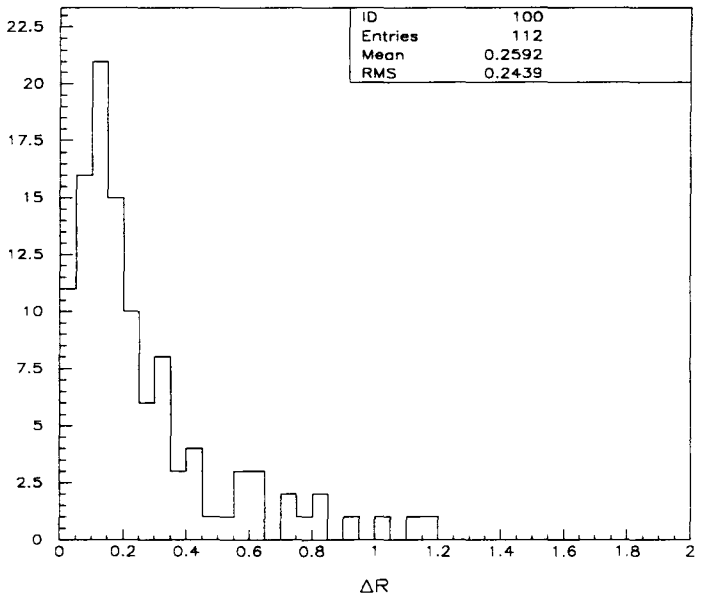

Figure 4-10. ΔR **distribution for data.**

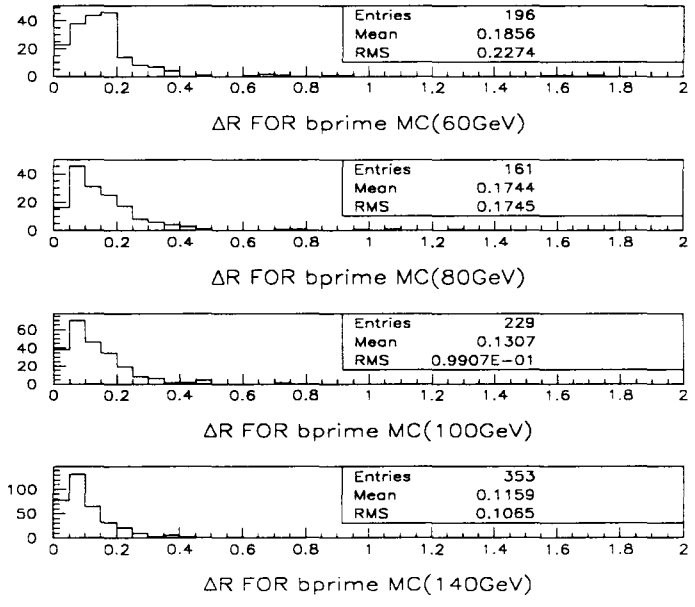

Figure 4-11. ΔR **distribution for ISAJET Monte Carlo.**

1. Triggers

The triggers used for this analysis are GIS_DIJET and JET_3_MON. The GIS_DIJET trigger is used for both signal and background data samples whereas JET_3_MON is used only for the background sample. Table 4-1 shows the level 1 and level 2 requirements of both the triggers.

Table 4-1. b' triggers(level 1 and level 2).

Trigger	Level 1	Level 2
GIS_DIJET	$\geq$ 1 EM tower $E_T > 10$GeV, $\mid \eta \mid < 2.5$ $\geq$ 1(HAD+EM) tower, $E_T > 3$GeV	1 isolated γ $E_T > 15$GeV, $\mid \eta \mid < 2.5$ $\geq$3 Jets(incl. γ), $E_T > 15$ GeV, $\mid \eta \mid < 2.0$ $H_T > 70$GeV using all jets in $\mid \eta \mid < 2.0$,
ELE_HIGH	$\geq$ 1 EM tower $E_T > 10$GeV	$\geq$ 1 EM tower $E_T > 20$GeV, one isolated EM cluster, $E_T > 20$GeV
JET_3_MON	$\geq$ 2(HAD+EM) towers, $E_T > 5$GeV	$\geq$ 3 Jets, $E_T > 10$GeV, $\Delta R = 0.3$
JET_MULTI	$\geq$ 3(HAD+EM) towers, $E_T > 7$GeV, $\mid \eta \mid < 2.6$	$\geq$ 5 Jets, $E_T > 10$GeV, $\Delta R = 0.3$,$\mid \eta \mid < 2.5$ $H_T > 100$GeV

2. Photon Selection

We require at least 1 photon in the event satisfying the following cuts.

- In photon identification there is no associated CD track.
- H-matrix χ^2 is < 100.
- EM fraction is > 0.95.
- Fractional isolation is < 0.1.

- $E_T > 20$ GeV.
- $|\eta| < 2.0$.

3. Jet Selection

Jets used in the analysis are reconstructed using the R = 0.5 cone algorithm. We require at least 3 jets in the event satisfying the following requirements : In the event selection we require

- $E_T > 15$GeV .
- $|\eta| < 2.0$.

Figure 4-12 and Figure 4-13 shows the E_T distribution of first, second, and third jets for signal Monte Carlo and data events respectively. Figure 4-14 and Figure 4-15 show the η distribution of all the jets for signal Monte Carlo and data events respectively.

4. Tagging Muon Selection

For this analysis we require an event to have at least one tagging muon satisfying the following requirements :

- Muons restricted to CF ($|\eta| < 1.0$).
- IFW4 ≤ 1.
- (HFRACT $\geq$ 0.75 and $ERACT_H(1) > 0$) OR (HFRACT = 1 and EFRACT_H(1) = 0).
- $\Delta R \leq 0.5$ and $p_T > 4$ GeV. ΔR is the distance in $\eta - \phi$ space between the muon and nearest 0.5 cone jet.

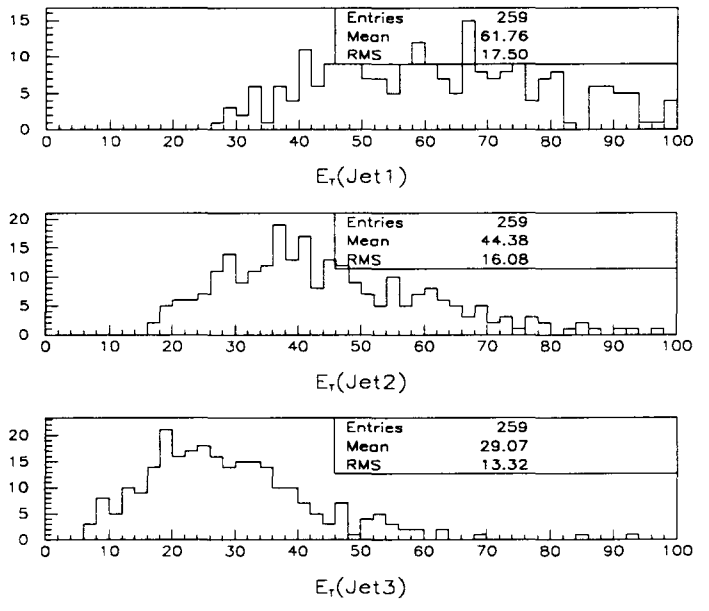

Figure 4-12. E_T distribution for first, second and third jet for signal Monte Carlo ($m_{b'} = 100$GeV).

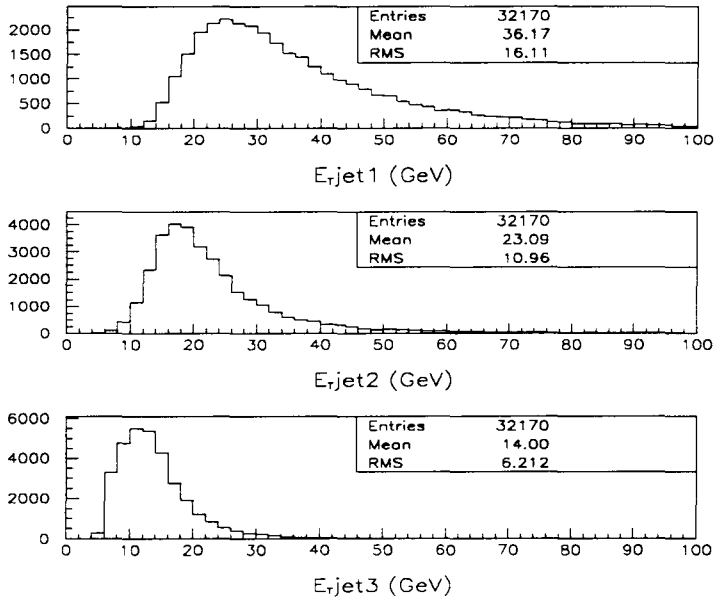

Figure 4-13. E_T distribution for first, second and third jet for data.

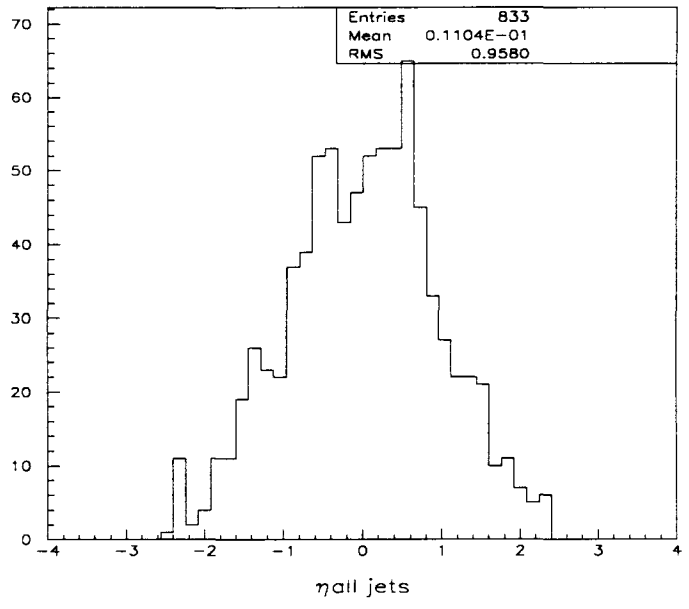

Figure 4-14. η distribution for all the jets for signal Monte Carlo ($m_{b'} = 100\text{GeV}$).

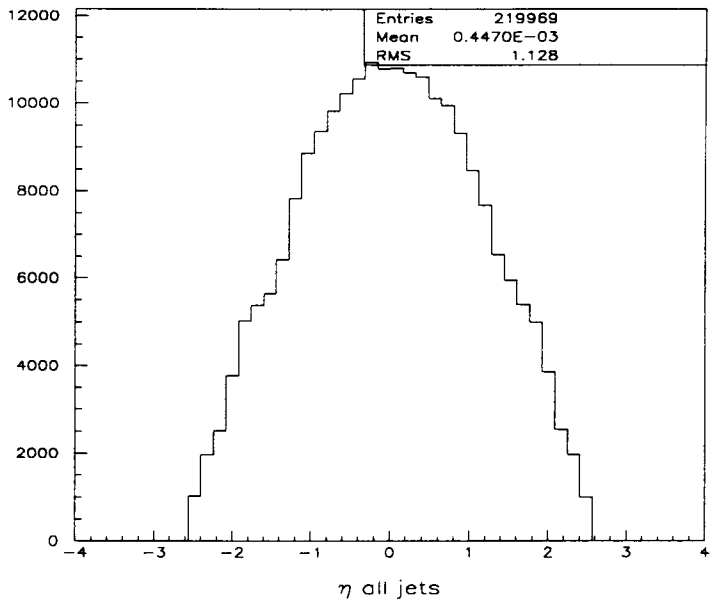

Figure 4-15. η distribution for all the jets for data.

5. H_T

H_T is defined as sum of the E_T's of the photon and all the jets, satisfying the above requirements. For this analysis we require:

- $H_T > 1.5 m_{b'}$

Here $m_{b'}$ is the b' mass for the Monte Carlo sample. Figure 4-16 shows the H_T distribution of Monte Carlo b' events. The dotted line shows the cut to be applied later. And Figure 4-17 shows the significance which is defined as $acceptance/\sqrt{background}$ as a function of the H_T for different b' masses.

D. Acceptance

The acceptance for the single photon decay mode was calculated by using the following formula.

$$acceptance = \frac{\#\ of\ events\ after\ applying\ the\ cut}{total\ no\ of\ events\ generated} \times\ total\ correction$$

For the acceptance we use HERWIG and ISAJET event generators where one b' is forced to decay to a photon and second b' quark decays to a gluon. The average of HERWIG and ISAJET is used to calculate the cross section. Table 4-2 gives the acceptance for several b' masses which includes the various corrections given in Table 4-3.

The errors in Table 4-2 include the systematic error from Table 4-3 and additional jet energy scale systematic errors obtained by looking at the change in acceptance, when we vary the energy scale corrections one standard deviation above and below the central value.

E. Background

The backgrounds for photon + jets come from

- QCD production of high-p_T direct photons plus multiple jets.

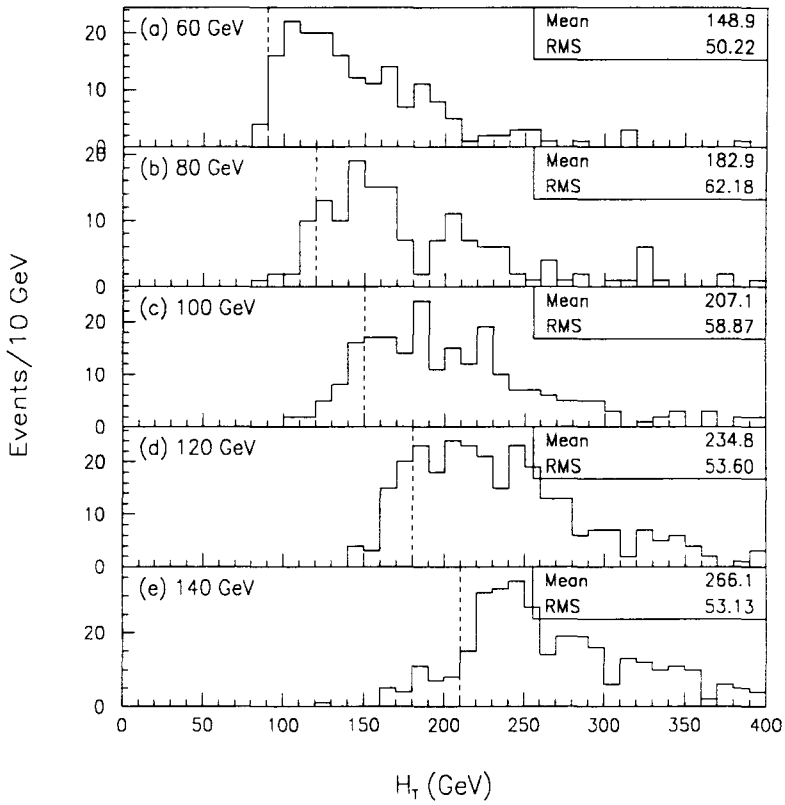

Figure 4-16. Monte Carlo b' H_T distribution for several different b' masses.

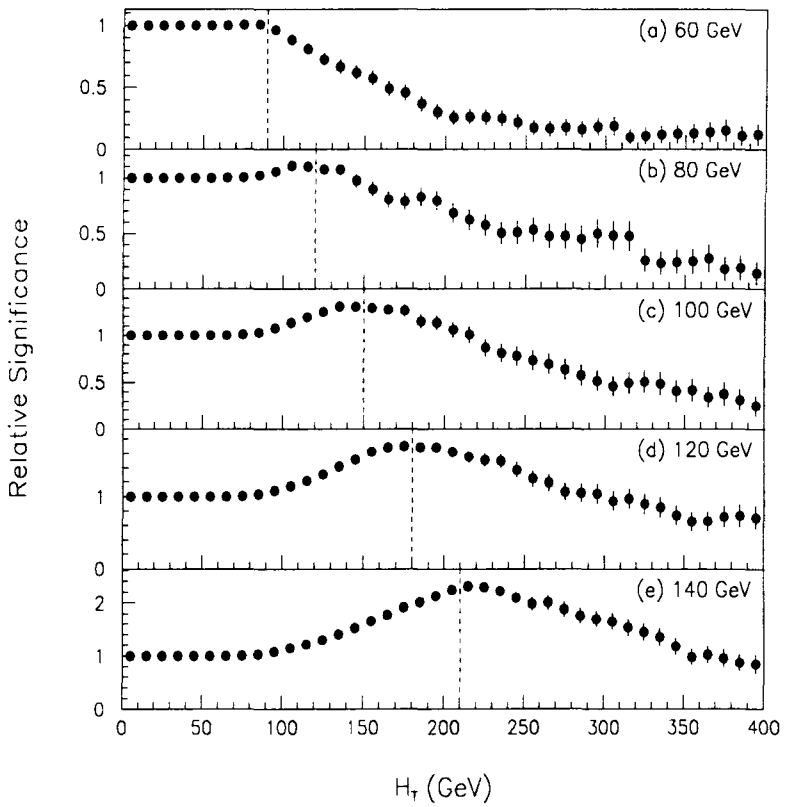

Figure 4-17. Relative Significance as a function of the H_T cut for several different b' masses.

Table 4-2. Acceptance for $b'\bar{b}' \rightarrow \gamma + 3jets + \mu - tag$ for different masses.

	Acceptance(%)		
$m_{b'}$	Herwig	Isajet	Average
50	0.270 ± 0.061	0.308 ± 0.069	0.289 ± 0.065
60	0.782 ± 0.141	0.697 ± 0.139	0.739 ± 0.140
70	1.170 ± 0.216	1.160 ± 0.212	1.165 ± 0.214
80	1.848 ± 0.353	1.441 ± 0.272	1.644 ± 0.312
90	2.335 ± 0.399	1.780 ± 0.318	2.057 ± 0.359
100	2.582 ± 0.443	2.227 ± 0.385	2.405 ± 0.414
120	3.446 ± 0.581	2.591 ± 0.488	3.028 ± 0.534
140	4.610 ± 0.678	3.666 ± 0.657	3.913 ± 0.667

- QCD multijet production with one jet misidentified as a photon.
- Diboson ($W\gamma$, $Z\gamma$)
- W or Z with electron misidentified as a photon.

The estimation of the two main backgrounds QCD production of high-p_T direct photons plus multiple jets and Diboson, is done by the tag rate method defined in the following section.

1. Tag Rate Function

The tag rate is the probability of finding the muon tagged jet in our sample. It can be defined as the number of tagged jets either per event or per jet:

$$Tag\ rate\ (per\ event) = \frac{number\ of\ tagged\ jet}{Total\ number\ of\ events}$$

$$Tag\ rate\ (per\ jet) = \frac{number\ of\ tagged\ jet}{Total\ number\ of\ jets}$$

The tag rate function per jet depend on the E_T and η of the jet, and is independent of number of jets. The tag rate per event however is proportional to

Table 4-3. Acceptance correction.

Effect	Correction Factor(%)
Generator	100 ± 10
Photon reconstruction	90 ± 2
Photon conversion	88 ± 1
HITSINFO efficiency	90 ± 5
Muon reconstruction	90 ± 10
Trigger efficiency	95 ± 5
Total correction	61 ± 10

the number of jets. The tag rate function is derived from JET_MULTI trigger data which is the largest available sample of low E_T jets.

a. Tag rate η dependance. The η dependance of the tag rate is shown in Figure 4-18 and given by following formula [21]:

$$R(\eta) = A[\mathrm{erf}\frac{(\eta + \eta_0)}{\sqrt{2\sigma_n}} - \mathrm{erf}\frac{(\eta - \eta_0)}{\sqrt{2\sigma_n}}]$$

The values of the parameters obtained by the fit are

$A = (0.567 \pm 0.011)\%$, $\sigma_n = 0.253 \pm 0.010$, $\eta_0 = 0.855 \pm 0.014$. The normalization parameter A is adjusted to $A = 1.84$ in the total tag rate function to give the η factor an average value of one for the control sample.

b. Tag rate E_T dependence. The E_T dependence of the tag rate function is shown in Figure 4-19 From the Figure we see that the tag rate is linearly dependent on E_T at low E_T and then it saturates at high E_T. The E_T dependence of the tag rate function is given by the following formula:

$$R(E_T) = AE_{T0} \tanh \frac{E_T}{E_{T0}}$$

where $A = (8.99 \pm 0.17) \times 10^{-5}$ and $E_{T0} = 81.5 \pm 5.47$ GeV

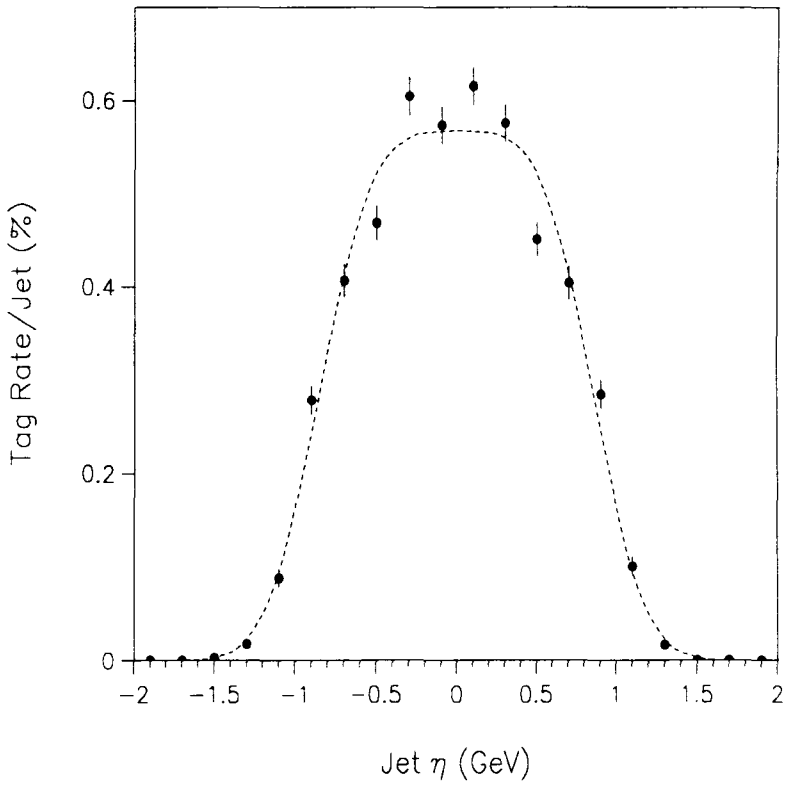

Figure 4-18. Tag rate per jet η dependence.

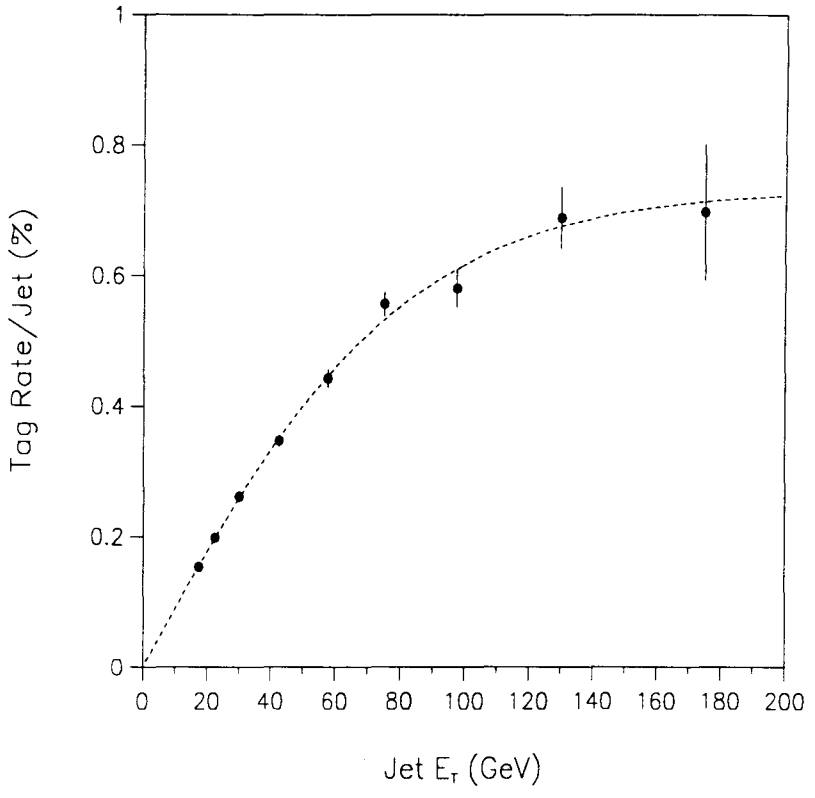

Figure 4-19. Tag rate per jet E_T dependence.

2. Background Calculation

The background calculation is based on 80% of the background tag rate which is calculated by the tag rate function. This factor comes from the average tag rate observed in the JET_3_MON three jet sample and the GIS_DIJET bad photon + three jet sample. It is reasonable to do this because these samples have similar triggers and kinematics which are more similar to the signal sample than the JET_MULTI sample from which the tag rate function is obtained. This calculation contributes a 20% systematic error to the tag rate. Figure 4-20 shows the H_T distribution for the various backgrounds. Figure 4-21 shows the signal and background H_T distributions for bad photon(jet misidentified as photon) + 3 jet events. Figure 4-22 shows the H_T distribution of actual signal and background. There is no obvious excess of signal over background.

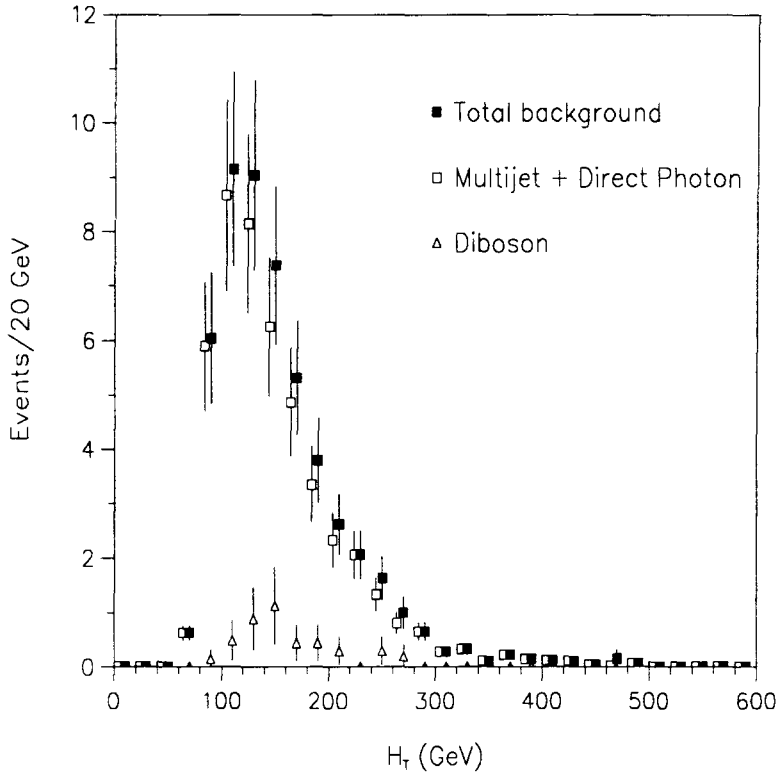

Figure 4-20. H_T **distribution for various background.**

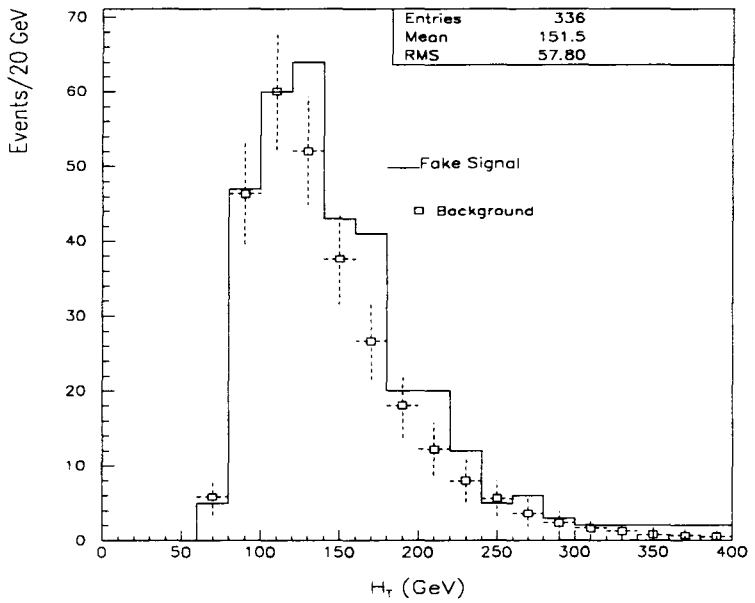

Figure 4-21. H_T distribution of fake signal and background in bad photon + 3 jet events.

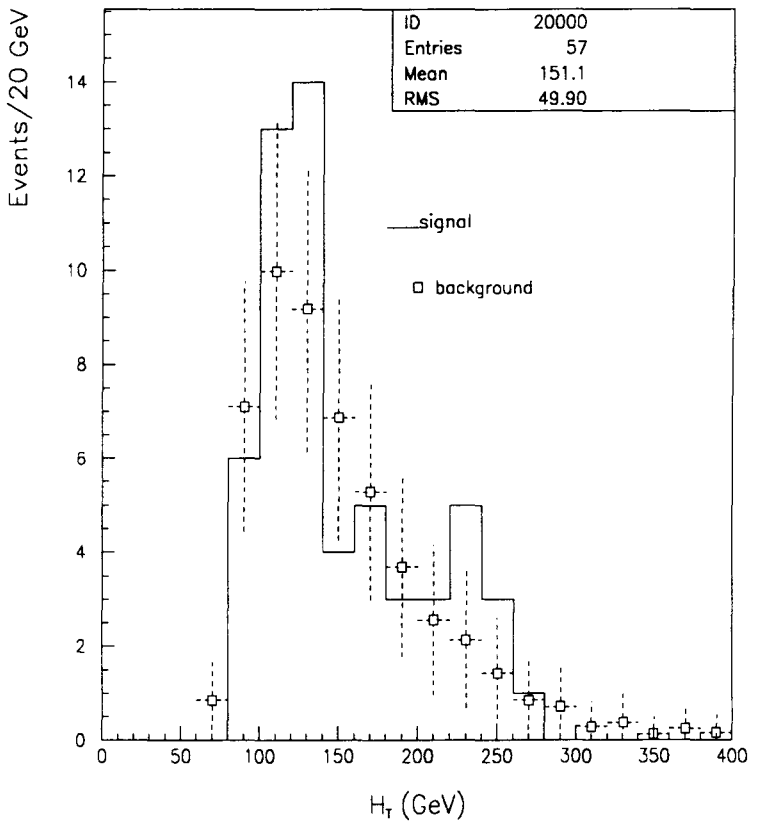

Figure 4-22. H_T distribution of data and background in photon + 3 jet events. The distribution can be compared to the the signal H_t distribution from monte-carlo in Fig. 4-16.

CHAPTER 5
CONCLUSIONS

A. Cross Section And Mass Limits

The results from this analysis are summarized in Table 5-1 and Table 5-2. Tables 5-1 and 5-2 show the number of observed events, the number of events expected for signal and background, and the calculated cross section times branching ratio as a function of b' mass before and after the H_T cut respectively.

Table 5-1. The number of expected and observed photon + 3 jet events as a function of b' mass before the H_T cut.

	Events			$\sigma_{b'\bar{b}'} \times BR(pb)$	
$m_{b'}$	Observed	Expected signal	Expected background	Value	upper limit (95% CL)
50	57	165±38	51±10	25.4±49.8	116
60	57	179±35	51±10	9.7 ±18.9	44.1
70	57	129±24	51±10	5.9 ±11.6	26.9
80	57	092±17	51±10	4.1 ±8.0	18.5
90	57	61 ±11	51±10	3.3 ±6.4	15.0
100	57	44 ±8	51±10	2.6 ±5.1	11.8
120	57	21 ±4	51±10	2.0 ±4.0	9.3
140	57	12 ±4	51±10	1.6 ±3.1	7.1

The expected number of events is calculated using the theoretical cross section of Laenen *et al.* [1], multiplied by the efficiency, branching fraction and

Table 5-2. The number of expected and observed photon + 3 jet events as a function of b'mass After the H_T cut.

	Events			$\sigma_{b'\bar{b}'} \times BR(pb)$		
$m_{b'}$	Observed	Expected signal	Expected background	Measured Value	upper limit (95% CL)	Theoretical Value
50	57	164±38	51±10	26.1±50.0	117	670.0
60	56	174±31	48±9	12.9±18.9	46.5	278.3
70	44	121±23	42±8	2.4 ±10.4	22.0	122.4
80	38	84 ±17	35±7	2.2 ±6.5	14.2	60.3
90	29	56 ±10	28±5	0.7 ±4.3	8.9	32.4
100	22	37 ±7	22±4	0.0 ±3.1	6.1	18.4
120	15	18 ±3	13±3	0.6 ±1.8	4.0	7.0
140	9	10 ±2	8 ±2	0.3 ±1.0	2.2	3.3

luminosity assuming the branching ratios BR($b' \rightarrow b\gamma$) = 10% and BR($b' \rightarrow bg$) = 90%, giving combined branching ratio of 18%.

We calculate the cross section times branching ratio according to the equation

$$\sigma_{b'\bar{b}'} \times BR = \frac{S - B}{A\mathcal{L}}$$

where S is the observed number of events, B is the expected background, A is the efficiency for a particular b' mass, and $\mathcal{L} = 84.5pb^{-1}$ is the integrated luminosity of the data set used in this analysis.

The error of the cross section times branching ratio is obtained by using propagation of errors assuming Gaussian error. The error of the integrated luminosity is 5.4%

There are two more methods in which similar results for $\sigma_{b'\bar{b}'} \times BR(pb)$ can be determined.

- By assuming the a particular branching ratio and determining the cross section as shown in Figure 5-1 which also compares the measured and

theoretical cross section as a function of b' mass

- By assuming the theoretical cross section and determining the branching ratio as shown in Figure 5-2 which shows the measured branching ratio as a function of b' mass

In both the cases 95% CL upper limit curve is obtained by using the actual gaussian likelihood for $\sigma > 0$.

From this analysis it can be concluded that b' decaying predominantly via flavor changing neutral currents into b quark is ruled out for b' mass less than Z boson mass.

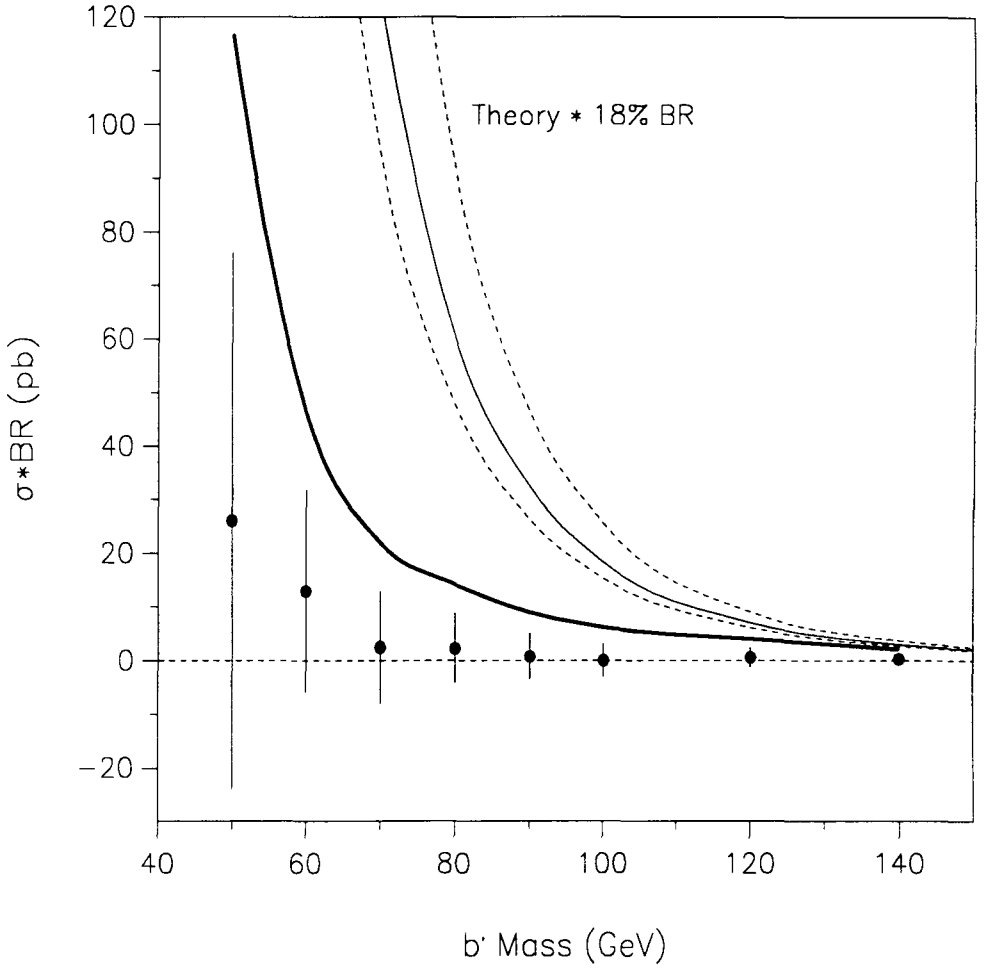

Figure 5-1. Comparison of measured cross section times branching ratio (points) and 95% CL upper limit (thick line) for $b'\bar{b}' \rightarrow \gamma + 3$jets with the theoretical cross section of Laenen *et al.* times an assumed branching ratio of 18%. The dashed theory curve are upper and lower limit curve for the theoretical cross section.

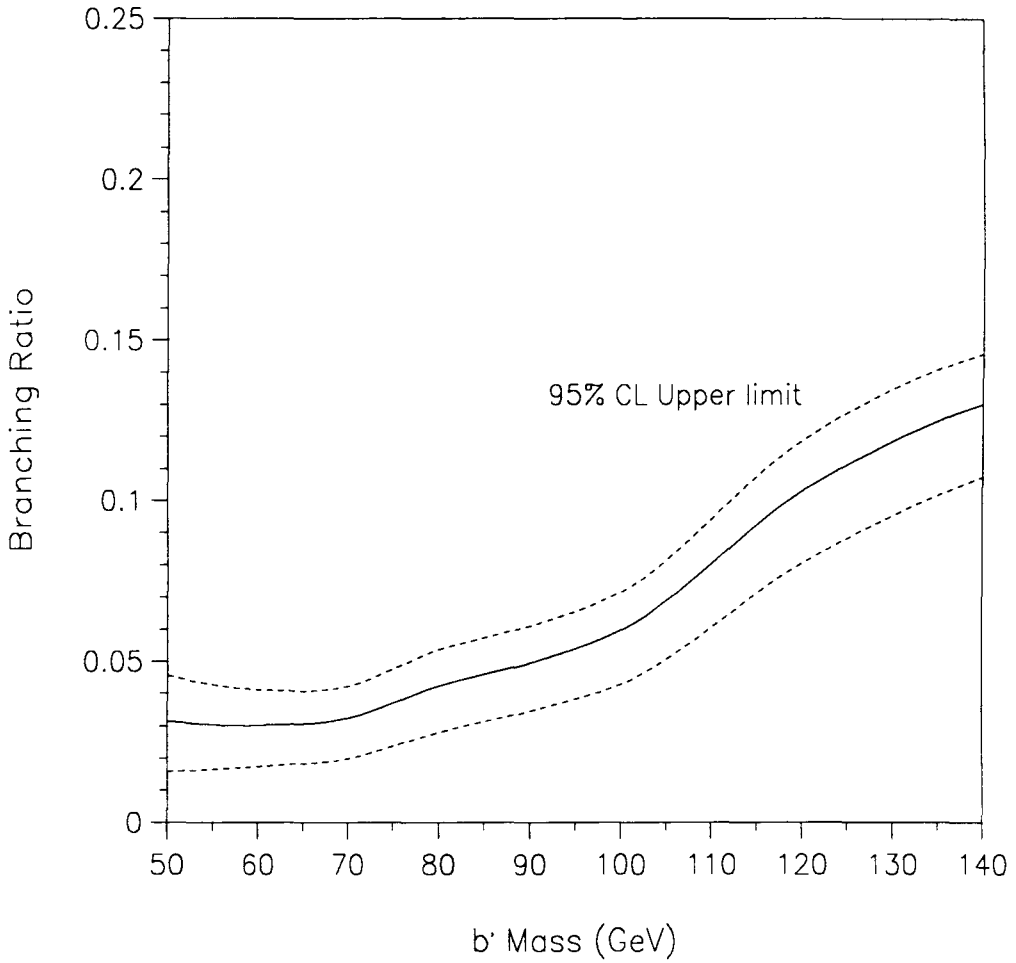

Figure 5-2. Measured 95% CL upper limit on the branching ratio for $b'\bar{b}' \rightarrow \gamma + 3$Jets assuming the theoretical cross section of Laenen *et al.*. The dashed curves are obtained using upper and lower limits on the cross section, rather than the central value.

BIBLIOGRAPHY

[1] E.Laenen,J.smith,W.van Neervan, Phys.Lett.321B, 254 (1994).

[2] E.Berger and H.Contopanagos, Phys.Lett.361B, 115 (1995).

[3] S.Catani, M.L.Mangano, P.Nason, and L.Trentadue, CERN-TH-96-21, jan.

[4] S.L.Glashow, J.Iliopoulos, and L.Maiani, Phys.Rev.D 2,1285 (1970).

[5] W.S.Hou, and R.G.Sturt, Phys.Rev.Lett.62,617(1989).

[6] DØ Collaboration, S. Abachi *et al.,* Nucl. Instrum. Methods, Phys. Res. Sect A 338, 185(1994).

[7] R. Wigmans, Nucl. Instr. and Meth. A 259, 389, (1987); *ibid* A 265, 53, (1986).

[8] DØ Collaboration, S.Abachi *et al.,*Physics.Rev.Lett. 72, 2138(1994).

[9] VENUS Collaboration, K.Abe *et al.,*Phys.Rev.Lett.63, 1776(1989). AMY Collaboration, S.Eno *et al.,*Phys.Rev.Lett.63, 1910 (1989). TOPAZ Collaboration, I.Adachi *et al.,*Phys.Rev.Lett.234 B, 197 (1990). ALEPH Collaboration, D.Decamp *et al.,*Phys.Rev.Lett.236B, 511 (1990).

[10] Particle Data Group, L.Montanet *et al.,*Phys.Rev.D 50, 1442 (1995).

[11] Particle Data Group, L.Montanet *et al.,*Phys.Rev.D 50, 1312 (1995).

[12] J.F.Gunion,D.W.McKay, and H.Pois, UCD-95-18,May 1995.

[13] W.S.Hou, Phys.Rev.Lett. 72, 3945 (1994).

[14] W.s. Hou and R.G. Stuart, Nucl.Phys.B320,277(1989).

[15] CDF Collaboration, F.Abe *et al.,*Phys.Rev.Lett.69.

[16] DØ Collaboration, J.A. Guida, in Proceedings of the 4th International Conference on Advanced Technology and Particle Physics, Combo, Italy, 1994 (unpublished);Fermilab Report No.FERMILAB-CONF-95/010-E,1995 (unpublished); DØ collaboration, J.Kocher, Fermilab Report No FERMILAB-CONF-95-E,1995(unpublished).

[17] F. Paige and S. Protopopescu, BNL Report No. BNL38034, 1986 (unpublished), release v6.49.

[18] G.Marchesini *et al.*,Comput.Phys. Commun. 67,465 (1992).

[19] A.J.Milder,PhD.thesis,University of Arizona,1993.

[20] P.Agrawal, W.S.HOu, Phys.Rev.D 46,1022 (1992).

[21] J. Butler, H. Greenlee, M. Narain, P. singh, DØ Note under preparation.

[22] Leon M. Lederman. The Tevatron. *Scientific American*, 264(3):48-55, March 1991.

[23] FNAL. Design report Tevatron 1 project. FNAL internal note, September 1984.